CFD Techniques for Simulation of Flow in a Scour Hole around a Bridge Pier

Md Nazmus Sakib

A Thesis

In

The Department

Of

Building, Civil and Environmental Engineering

Presented in Partial Fulfilment of the Requirements

For the Degree of Master of Applied Science (Civil Engineering) at

Concordia University

August 2013

CONCORDIA UNIVERSITY
School of Graduate Studies

This is to certify that the thesis prepared

By: Md Nazmus Sakib

Entitled: CFD techniques for simulation of flow in a scour hole around a bridge pier

and submitted in partial fulfillment of the requirements for the degree of

Master of Applied Science

complies with the regulations of the University and meets the accepted standards with respect to originality and quality.

Signed by the final examining committee:

Dr. M. Zaheeruddin Chair

Dr. L. Kadem Examiner

Dr. F. Haghighat Examiner

Dr. S. Li Supervisor

Dr. A. Zsaki Supervisor

Approved by _____
Chair of Department or Graduate Program Director

_____
Dean of Faculty

Date _____

Abstract

CFD Techniques for simulation of flow in a scour hole around a bridge pier

Md Nazmus Sakib

The flow field around a bridge pier is complex in detail and the complexity is further increased with the development of a scour hole. As flow-induced scouring around piers can cause bridge failures, a good understanding of the flow field is important to the safe design of the hydraulic structures. The objective of this study is to simulate free-surface flow around a pier in a fixed scour hole, and to further determine shear stress distributions at the channel-bed. Simulations were mainly performed using mesh-based numerical models. The mesh-based numerical model was established using Reynolds averaged momentum and continuity equations in three dimensions, with the k-ω model for turbulence closure. The regions around the pier and near the channel-bed were resolved with sufficiently fine mesh so as to capture detailed velocity structures. To explore the appropriate procedures for applying smoothed particle hydrodynamics, a mesh-free model was formulated with kernel approximation of the field variables and particle approximation. The governing equations for dynamic fluid flows for the mesh-free model were written as a set of partial differential equations in Lagrangian description, known as the Navier-Stokes equations. The simulations were carried out under the same geometric and hydraulic conditions as in available laboratory experiments. One of the major findings of this research is that, both models predict a downflow near the upstream nose of the pier which would affect the stability of pier foundations. The mesh-based model results

exhibit realistic vortex features around the pier and in the wake region. Another new finding is the occurrence of flow separation and complex vortex stretching confined to the upper water column behind the pier. The predicted bed shear stress and turbulent kinetic energy are shown to compare well with the experimental data. Application of the mesh-free model to the flow in a scour hole around a bridge pier has been successful in generating desired approach flow. Velocity profiles extracted from the results of both models at selected locations in the approach channel, inside the scour hole, are compared. The results presented in this thesis are of practical values for prediction of sediment scour around bridge piers.

ACKNOWLEDGEMENT

First of all, I would like to express my gratitude to my supervisors Dr Samuel Li and Dr Attila Zsaki. The guidance, support and encouragement they provided throughout the research are greatly appreciated. Their invaluable assistance and abundant help in preparing my thesis are highly appreciated. I am fortunate enough to have such excellent mentors and I take this opportunity to thank them for their support.

Also, I would like to thank the examiners Dr. Lyes Kadem, Dr. Fariborz Haghighat and the Thesis Committee chair Dr. Mohammed Zaheeruddin, for their comments and suggestions that helped to prepare the version of this thesis.

This research project would have not been possible without the financial support received from Dr S. Li and Dr. A. Zsaki.

Last but not the least; I would like to thank my parents, my family members and friends for their endless love and support through the whole duration of my studies.

Table of Contents

LIST OF FIGURES

LIST OF TABLES

LIST OF SYMBOLS

B= Channel width on both sides of the pier (m)

D= Pier diameter (m)

C= Log-layer constant (N-m)

c= Speed of sound (m/s)

c_o= Reference speed of sound in water (m/s)

e= Internal energy (-)

F= Volume fraction (-)

F_a= Volume fraction of air (-)

F_w= Volume fraction of water (-)

F_r= Froude Number (-)

g= Acceleration of gravity (m/s^2)

h= Smoothing length (m)

h_o= Initial depth outside the scour hole (m)

k= Turbulent kinetic energy (m^2/s^2)

κ= Von karman constant (-)

L_1= Channel length upstream of the pier (m)

L_2= Channel length downstream of the pier (m)

N= Number of particles (-)

p= Instantaneous pressure component (N/m^2)

P= Reynolds-averaged pressure (N/m^2)

p'= Turbulent fluctuation component of pressure (N/m^2)

Pr= Turbulence production term (-)

Q= Discharge (m^3/s)

q= Discharge per unit width (m^2/s)

R_e= Reynolds Number (-)

S_{ij}= Mean flow strain rate ($\frac{1}{s}$)

t= Time (s)

W= Smoothing kernel function (-)

Δt= Time step (s)

u= Instantaneous velocity component in x direction (m/s)

U= Mean velocity component in x direction (m/s)

u'= Velocity fluctuation component in x direction (m/s)

u^+= Near wall velocity (m/s)

u_τ= Frictional velocity (m/s)

u^*= Shear velocity (m/s)

U_t= Velocity tangent to the wall (m/s)

Un_w= Velocity normal to the wall (m/s)

u_o= Depth averaged approach flow velocity (m/s)

v= Instantaneous velocity component in y direction (m/s)

V= Mean velocity component in y direction (m/s)

v'= Velocity fluctuation component in y direction (m/s)

w= Instantaneous velocity component in z direction (m/s)

W= Mean velocity component in z direction (m/s)

w'= Velocity fluctuation component in z direction (m/s)

y^+= Dimensionless distance from the wall (-)

Δy= Distance from the wall (m)

ε= Turbulent dissipation rate (m^2/s^3)

ρ_o= Reference water density (kg/m^3)

ρ_a= Density of air (kg/m^3)

ρ_w= Density of water (kg/m^3)

τ= Viscous stress (N/m^2)

τ_{ij}= Reynolds shear stress tensor (N/m^2)

τ_w= Wall shear stress (N/m^2)

σ= Total stress tensor (N/m^2)

μ= Dynamic viscosity of water (Ns/m^2)

ω= Energy dissipation per unit k ($\frac{1}{s}$)

ν_t = Turbulent eddy viscosity (m^2/s)

Chapter One Introduction

1.1 Background

Water flows in an open channel naturally along its path under the influence of gravity. When there is an obstacle in the flow path, the flow changes direction in response to the obstacle. Such an instance can be the flow pattern in a channel with a cylinder inside the channel. As flow cannot proceed through the solid cylinder, it improvises its reaction bringing some changes in its path. This case resembles the flow in an open channel with a bridge pier.

For providing means of transportation over river channels, bridges are constructed across rivers. Bridges stand on piers and piers embedded in the channel bed bear the load from the bridge. The stability of piers safeguards the stability of bridges. Modification in flow pattern around a pier results in channel-bed alteration and this phenomena is defined as local scour. The flow field around a pier is complex in detail and the complexity is aggravated with the development of scour hole. Scouring lowers the bed level around piers creating hole and threatens the stability of bridge foundations which yield bridge failures. It has been well-documented that bridge pier scouring has been a significant transportation problem (Shirole and Holt, 1991). A good understanding of the flow field is essential for safe pier-foundation design.

The complex process of scour development is poorly understood as evident from the literature survey presented in the next chapter. To improve our understanding, a more detailed description of the flow field must be obtained.

Although the flow problem has been extensively studied in the past, our ability to predict the flow for given conditions is still limited due to various intricate secondary flow induced in scouring.

The turbulent flow around a bridge pier in an open channel is very complicated with vortices and eddy motions of various time and length scales. The flow characteristics are highly variable due to different types of piers and channel bed geometry. With a small variation of turbulence and channel geometry, the scouring induced by flow becomes erratic in many folds. In three-dimensional turbulent flow, the number of unknowns is more than the number of equations that can be established to solve for the unknowns (Wilcox, 1994). Thus analytical solutions are very difficult to attain where such complex turbulent flows are evident due to scouring. Field studies and experiments are very expensive. Numerical modelling represents a good alternative approach.

Bridge piers with cylindrical shape (circular cross section) are the most general pier. As the flow goes around a pier, bed sediments from the flat bed geometry are often eroded. These eroded sediments again settle down slowly around the pier. The scouring rate is higher than the sediment settling rate at the beginning and at equilibrium both erosion and settling of sediments reaches a steady rate. The initially higher rate of scouring results in equilibrium fixed scour hole around a pier.

This numerical modelling research considers the bridge hydraulics problem where three-dimensional (3-D) open-channel flow approaches a fixed scour hole and interacts with a circular pier. The purpose of this research is to investigate the complex three-dimensional velocity field as a result of the interaction, which is

difficult to measure in the laboratory and the field. The understanding of flow field around a pier is one of the most important aspects of bridge hydraulics. Flow approaching a bridge pier has tendency to move downward towards the channel bed which has implication in removing sediments from the channel bed. Excessive sediment removal or scouring is alarming for the safety of the bridge pier, which can eventually lead to uprooting of pier from the channel bed and yield bridge failure. So accuracy in the ability to predict local scouring around a bridge pier brings more confidence in safe pier-foundation design.

A major part of this thesis is to use a traditional finite element method to investigate flow field. A relatively new modelling technique will also be used as a complementary. The specific objectives are described below:

1.2 Objectives

The objectives of this thesis are:

- to numerically simulate detailed 3-D flow structures, including vortices and eddy motions, around a circular bridge pier using the mesh-based finite element method (FEM) (CFX, ANSYS® Academic Research, Release 14.0).
- to verify the simulated flow field with available laboratory measurements.
- to explore the appropriate procedures for applying the mesh-free method in smoothed particle hydrodynamics (SPH) (Crespo et al. 2011 and Gómez-Gesteira et al. 2012a, 2012b) to simulate flow in a scour hole around a bridge pier.

1.3 Scope of the work

To achieve the above-mentioned objectives, the rest of this thesis is organized as follows.

Chapter Two gives a summary of previous studies reported in the literature, on the topic of flow around bridge piers, including experimental and analytical studies on flow dynamics and the formation of turbulent eddies. Previous studies using different numerical solvers to resolve the flow field around piers with different pier shape and channel geometry will be reviewed. Progress made from the previous studies and outstanding issues will be discussed.

Chapter Three describes the modelling methodologies used in this study. The description will cover fundamental concepts and theory in CFD modelling of free surface flow. This chapter begins with the Reynolds-averaged momentum and continuity equations in three dimensions, along with the k-ω model for turbulence closure in mesh-based FEM modelling, and then discusses the formulations in SPH. Parameters involved in the modelling methods will be discussed.

In Chapter Four, the model channel and setup of both the mesh-based FEM (CFX, ANSYS® Academic Research, Release 14.0) and mesh-free SPH simulations will be discussed. Details of boundary condition, initial condition, control parameter and their values (e.g. turbulence intensity, time stepping and kernel function) will be explained. Also, considerations of model domain dimensions for both FEM and SPH will be given.

Chapter Five is devoted to presentation of the results from both FEM and SPH simulations. Analyses of the acquired data from the models will be further

conducted. A direct comparison between the FEM model results and experimental results from Graf and Istiarto (2002) will be made.

Finally in Chapter Six, the advantages and limitations of FEM and SPH in application to the bridge hydraulics problem will be discussed. Conclusions from the application will be drawn. Suggestions for future research on the topic of numerical modelling of scour-inducing flow around bridge piers will be made.

1.4 Contributions from the work

This research work has made significant contributions as described below:

- stimulating exploration with diverse modelling tools for an unresolved issue in bridge hydraulics application.
- generation of a significant amount of data of flow velocity in a scour hole, which are useful for understanding and predicting scour induced flow around bridge piers.
- demonstration of reliable prediction tools for extrapolation of expensive laboratory measurements.
- aiding guidance to apply the simulation methods for solving more complex problems in bridge hydraulics application.

Chapter Two Literature Review

2.1 Bridge scour processes

The local scour around bridge piers is one of the most common causes of bridge failures (Richardson and Davis, 2001). The fully three-dimensional flow around a cylindrical (circular in cross section) pier situated in a scour hole is schematically described in Figure 2.1 (Richardson and Davis, 2001). As the flow approaches the pier at the upstream side, the part of the flow in front of pier decelerates and is deflected upward and downward direction. The upward flow near the free surface forms a circulation called the bow wave. Due to flow acceleration around the pier, the free surface is drawn down. As the flow in the middle of the water column approaches the pier, due to the obstacle, the flow has to pass around the pier. A portion of the separated flow moves down, towards the bottom along the upstream face of the pier. This downward flow, driven by a strong pressure gradient, induced by velocity gradient interacts with the bed material and forms a horseshoe vortex at the base. These vortices with a horizontal axis of rotation remove bed material from the base at a greater rate of material transported to this region resulting in scour holes (Richardson and Davis, 2001). With increasing scour depth, the horseshoe vortex loses its strength and live bed local scour turns into equilibrium scour (Richardson and Davis, 2001). As the flow converges at downstream of the pier, wake vortices form with vertical axis of rotation. The wake vortices cause strong circulation throughout the entire flow depth forming a wake region behind the pier. Both the

horseshoe and wake vortices remove material from the base of pier (Richardson and Davis, 2001).

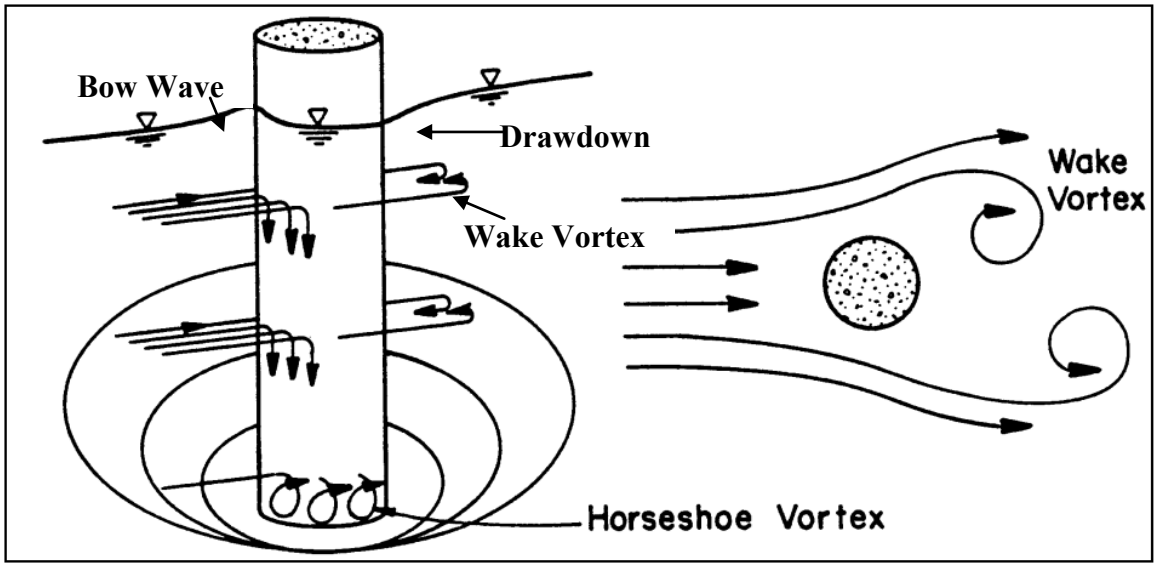

Figure 2.1 Schematic representation of flow around a circular pier (Richardson and Davis, 2001).

2.2 Experiments of bridge pier scour

Previously, investigators have made extensive laboratory measurements of flow velocity around piers, along with turbulence, bed shear stress and vortex shedding. Breusers *et al.* (1977) and Richardson *et al.* (1993) addressed the complexity in analysis of local scour at bridge pier as it requires various formulas that involve descriptions of mean flow field. Their application to complex flow patterns is problematic and often leads to questionable results in field applications, according to Landers and Mueller (1996). Laboratory and field investigations are time consuming and expensive. Due to recent advances, numerical solutions are increasingly considered to be a more reliable approach (Dargahi, 1987).

Melville (1975) conducted extensive measurements of the flow field, turbulence, bed shear stress and vortex shedding in the small-scale laboratory experiments with circular piers for rigid flat bed, intermediate scour hole and equilibrium bed. Dargahi (1987) presented detailed measurements for velocity, pressure, horseshoe vortex and bed shear stress. Yanmaz and Altinbilek (1991) performed sets of experiments using single cylindrical and square bridge pier models in the laboratory under clear water conditions with uniform bed materials. Semi empirical time-dependent analysis of local scour depths around bridge piers has been conducted using the sediment continuity equation for the scour hole around bridge piers. For design purposes, non-dimensional scour prediction curves were prepared in terms of various sediment and flow properties. Ahmed (1995) and Ahmed and Rajaratnam (1998) performed detailed measurement of flow field and turbulent boundary layer in front of circular piers. Sarker (1998) conducted extensive laboratory experiments for the flow field in front and behind of small-scale circular piers using the acoustic Doppler velocimeter. Beheshti and Ataie-Ashtiani (2010) experimentally investigated three-dimensional turbulent flow field around a complex bridge pier placed on a rough fixed bed. The complex pier foundation consisted of a column, a pile cap, and a 2x4 pile group where all the elements were exposed to the approaching flow. An acoustic Doppler velocimeter was used to measure instantaneously the three components of the velocities at different horizontal and vertical planes. Graf and Istiarto (2002) conducted experiment of the three-dimensional flow field in an established (equilibrium) scour hole and vorticity was calculated based on the measured instantaneous velocity components.

All the investigations have contributed to an improved understanding of the intricate scour process. They have also produced some useful empirical methods mainly for determining the maximum depth of scour, which is indeed of practical importance to the safe and cost-effective design of bridge piers. However, experimental investigations have an inherent limitation – that is the use of typically small-scale laboratory flumes. There are uncertainties in terms of artificial boundary effects and scaling; either Reynolds number or Froude number similarity has to be ignored due to difficulties in meeting both similarity laws.

2.3 Three-dimensional modelling of bridge pier scour

Mendoza-Cabrales (1993) used the standard *k-ε* turbulence model to solve three-dimensional flow in the vicinity of vertical circular piers and computed the associated bed shear stress but a large discrepancy was found compared to the experimental data of Melville (1975). Olsen and Malaaen (1993) used a steady state Navier-Stokes solver coupled with a sediment transport algorithm to simulate the growth of scour hole at the base of a circular pier. Ali et al. (1997) showed that the renormalization group (RNG) *k-ε* model gives a good estimation of the velocity field and bed shear stress. Dey et al. (1995) developed a three-dimensional semi-empirical kinematic model for vortex flow around circular piers in a quasi-equilibrium scour hole in a clear water regime. The velocity distribution pattern obtained by Melville (1975) matched satisfactorily with the model output results. Dou et al. (1998) calculated the anisotropic turbulence stresses and the associated bed shear stresses using the turbulence Reynolds stress model developed by Dou (1980).

Richardson et al. (1998) used a CFD model called FLOW-3D developed by Sicilian et al. (1987). The FLOW-3D model solves three-dimensional transient Navier-Stokes equations by the volume-of-fluid method developed by Hirt and Nicholas (1981). The model supported turbulent closure through a number of schemes including Prandtl's mixing length theory, the eddy viscosity model, the two equation k-ε model and the renormalized group (RNG) theory. The model output resulted in favorable qualitative and quantitative comparisons with experimental results by Melville and Raudkivi (1977). However Richardson et al. concluded that fairly dense grid resolution and good representation of pier and scour hole geometry had been necessary for better simulations of eddy motions.

Salaheldin et al. (2004) examined the performance of several turbulence models in simulating three-dimensional separated vertical flow field around circular piers utilizing a CFD solver FLUENT (FLUENT, 1998). Several variants of k-ε model and Reynolds stress model (RSM) has been used for turbulence closure. The computed velocity field and bed shear stress have been compared with some of experimental data available in literature like Melville (1975), Dargahi (1987) and Ahmed and Rajaratnam (1998). It appears that the standard and the RNG k-ε models are adequate for simulating the flow field around piers, but overestimate the near bed velocity. Reportedly, the Reynolds stress model gives the most acceptable results of velocity, bottom shear stress and water level in the case of flat bottom, and of velocity and water level in the case of equilibrium scour.

Huang et al. (2008) conducted numerical simulations to investigate the scale effect on turbulence flow and sediment scour near cylindrical bridge pier using FLUENT (ANSYS, 2007). Effect of scale on turbulence flow and sediment scour had

been investigated by comparing different results obtained from full scale numerical model to those derived from Froude similarity method. In physical modeling either Reynolds or Froude similarity has to be ignored due to difficulty in meeting both similarity laws. But in this study using three-dimensional CFD model, both Froude and Reynolds number effects had been included. Though obtaining perfect results had been difficult due to many factors involved, Huang et al. concluded that the predicted flow patterns around the pier using FLUENT had exhibited good qualitative results.

Kirkil et al. (2008) conducted a study applying Large Eddy Simulation (LES) modeling aided by a laboratory experiment that aimed at delineating the coherent turbulence structures and their interactions in a scour hole formed at a circular cylinder founded in an alluvial bed at a relatively low Reynolds number for which Clearwater scour conditions persisted. The study report concluded that, the structure of the horseshoe vortex system was found to be more complex than previously indicated in scour literature. The numerically derived distribution of time-averaged bed-friction velocity around the cylinder had been found to concur with the equilibrium scour-hole bathymetry measured during the laboratory experiment.

2.4 Hydrodynamics applications of the SPH model

Monaghan (1992) applied the SPH (smoothed particle hydrodynamics) method for free surface incompressible flows phenomena such as dam-break, bore, wave maker and propagation of waves towards a beach. He found that the SPH method can simulate free surface flow without problems when given that the density is calculated approximating its rate of change and particles move with corrected

velocity. SPH being an explicit numerical method, Monaghan concluded that use of an artificial equation of state makes the time step shorter than desirable.

Randles and Libersky (1996) made improvements and changes in SPH for both fluids and solids. The use of kernel renormalization and conservative smoothing method, the instability and poor accuracy issues of SPH method have been improved. The study concluded that fluid-structure interaction model being more robust and incorporating the void treatment for multiphase flow, has made the SPH method simpler to apply.

Gomez-Gesteira and Dalrymple (2004) modeled the impact of a single wave generated by a dam break with a tall structure using three-dimensional SPH model. Both the effects of having dry and wet bed in front of dam prior to dam break have been discussed in this study. The velocity field at a given position and force exerted by the wave on the structure have been successfully reproduced. The simulated velocity fields have also compared well with experimental results.

Shao (2005) simulated non-linear and dispersive solitary wave reflection and transmission characteristics after interacting with partially immersed curtain-type breakwater using the SPH method. The model easily tracked free surfaces by Lagrangian particles without numerical diffusion. Partially immersed curtain breakwaters have been found effective in dissipating incoming wave energy when the immersion depth was over half of the water depth. The wave force on the curtain wall reached only one single peak value in case of smaller waves and double peak value in case of larger non-linear waves.

Dalrymple and Rogers (2006) examined the propagation of highly nonlinear and breaking waves with the improved SPH tool implementing a different time

stepping algorithm. The improvements made the SPH method to easily take care of turbulence, fluid viscosity and density. The method has performed very well for relatively small regions with lower number of particles. It was also concluded that the SPH method may not be suitable for larger number of particles.

Silvester and Cleary (2006) performed a three-dimensional dam-break flow and its interaction with a rectangular column downstream using the SPH model varying different simulation parameters. The results compared well with the existing experimental data. Crespo *et al.* (2007) studied the mitigation of force and moment exerted on structures by dikes with the three-dimensional SPH model. Interaction between both the water overtopping and flowing around the dike were found to be responsible for the force on the structure. The study concluded that the Lagrangian nature of SPH method permits the flow discontinuities without constraints due to presence of a grid.

Crespo *et al.* (2008) further analyzed the dam break evolution over dry and wet beds. The measured velocities from the two-dimensional SPH model reproduced the experimental dam break profiles accurately. It was found that although breaking dominates over wet beds in the beginning of movement, bottom friction turns into the principal dissipation mechanism later on. Staroszczyk (2010) simulated the two-dimensional dam break problem applying a SPH method with corrected smoothing kernel functions. The results from this exhibited better quantitative predictions of the wave front, with respect to time, than the standard SPH method.

Gomez-Gesteira *et al.* (2010) described the state-of-art of the classical SPH formulation of free surface flow phenomena such as two-dimensional and three-dimensional dam-break situations. Use of density filters and kernel correction for the

improvement of classic SPH approach has been performed. The study concluded that achieving higher accuracy depends on high number of particles with very small time steps. They suggested that combining SPH with other techniques to form hybrid methods that might speed up computation. Groenenboom and Cartwright (2010) applied coupling of SPH and Finite Elements (FE) to fluid-structure interaction for the case of dam break in a container and drop of flexible cylinder in water. The robustness and versatility of the physics-based SPH-FE fluid-structure interaction results have demonstrated the maturity of the hybridized solver over stand-alone SPH solver.

Takbiri *et al.* (2010) analysed the seepage through dam foundation using SPH method. Comparison of seepage maps and results obtained from both SPH and FE methods were performed in this study. Chang *et al.* (2011) described application of a numerical mesh-free method which solved the shallow water equations based on SPH technique for dam-break flow simulation in one-dimensional open channels. Proposed methods have been validated conducting different problems. The models had produced accurate solutions that compared well with experimental and field data.

Hopton (2010) attempted to convert Hydra, the pre-existing SPH code for astrophysical simulations to simulate water flow phenomena such as dam bursting and flow over a weir. The study concluded that SPH method and Hydra accurately reproduced the flow characteristics of dam break problem. With increasing complexity in boundaries, the commercial package ANSYS CFX had achieved better solution than Hydra.

Vacondio *et al.* (2012) simulated flood inundation using a SPH model for shallow water equations (SWEs) implementing the open boundary conditions for the first time. The results have been found in good agreement with the results of commercial software TUFLOW and a finite volume scheme. The study concluded that the SPH-SWE numerical model can be successfully applied to flooding over initially dry and complex bathymetries.

Edge *et al.* (2012) applied SPH on Nvidia CUDA-enabled graphics card (GPUSPH) for modeling wave runup and overtopping applications. The best part of this method has been that GPUSPH allows the incorporation of very irregular bathymetry. The model results had shown good comparison with other numerical and experimental results. The study concluded that GPUSPH did not require much time for this simulation and this simulation time lowered with increasing cores in Nvidia graphics cards.

Chapter Three Modelling Theories

This chapter provides a description of the mesh-based FEM model (CFX, ANSYS® Academic Research, Release 14.0) and mesh-free SPH model (Crespo et al. 2011 and Gómez-Gesteira et al. 2012a, 2012b). The description covers the governing equations, turbulence closure, boundary conditions imposed and model setup.

3.1 The FEM model

3.1.1 Governing equations

Let (u, v, w) denote the three orthogonal components of the instantaneous velocity in the x, y and z directions. For an incompressible fluid, the continuity equation is of the form

$$\frac{\partial u}{\partial x}+\frac{\partial v}{\partial y}+\frac{\partial w}{\partial z}=0 \tag{3.1}$$

where the z-axis points positively upward.

Through Reynolds decomposition, the instantaneous velocity components are split into mean velocity components (U, V, W) and velocity fluctuations (u', v', w') as below

$$u=U+u' \tag{3.2}$$

$$v=V+v' \tag{3.3}$$

$$w=W+w' \tag{3.4}$$

Since the average of individual velocity fluctuations are zero, the substituting equations (3.2)-(3.4) into equation (3.1) results in the Reynolds-averaged continuity equation of the form

$$\frac{\partial U}{\partial x}+\frac{\partial V}{\partial y}+\frac{\partial W}{\partial z}=0 \tag{3.5}$$

The momentum equations for an open channel can be expressed as

$$\rho\left[\frac{\partial u}{\partial t}+\frac{\partial}{\partial x}(uu)+\frac{\partial}{\partial y}(vu)+\frac{\partial}{\partial z}(wu)\right]=-\frac{\partial p}{\partial x}+\mu\left(\frac{\partial^2 u}{\partial x^2}+\frac{\partial^2 u}{\partial y^2}+\frac{\partial^2 u}{\partial z^2}\right) \tag{3.6}$$

$$\rho\left[\frac{\partial v}{\partial t}+\frac{\partial}{\partial x}(uv)+\frac{\partial}{\partial y}(vv)+\frac{\partial}{\partial z}(wv)\right]=-\frac{\partial p}{\partial y}+\mu\left(\frac{\partial^2 v}{\partial x^2}+\frac{\partial^2 v}{\partial y^2}+\frac{\partial^2 v}{\partial z^2}\right) \tag{3.7}$$

$$\rho\left[\frac{\partial w}{\partial t}+\frac{\partial}{\partial x}(uw)+\frac{\partial}{\partial y}(vw)+\frac{\partial}{\partial z}(ww)\right]=-\frac{\partial p}{\partial z}+\mu\left(\frac{\partial^2 w}{\partial x^2}+\frac{\partial^2 w}{\partial y^2}+\frac{\partial^2 w}{\partial z^2}\right) \tag{3.8}$$

where ρ is the density of water; t is the time; μ is the dynamic viscosity of water and p is the instantaneous pressure field. The instantaneous pressure p is decomposed into average value P and turbulent fluctuation p’ as

$$p=P+p' \tag{3.9}$$

Substituting equations (3.2)-(3.4) and (3.9) into equations (3.6)-(3.8) yields the Reynolds-averaged momentum equations

$$\rho\left[\frac{\partial U}{\partial t}+\frac{\partial}{\partial x}(UU)+\frac{\partial}{\partial y}(UV)+\frac{\partial}{\partial z}(UW)\right]=-\frac{\partial P}{\partial x}+\mu\left(\frac{\partial^2 U}{\partial x^2}+\frac{\partial^2 U}{\partial y^2}+\frac{\partial^2 U}{\partial z^2}\right)$$
$$-\rho\left[\frac{\partial}{\partial x}\left(\overline{u'u'}\right)+\frac{\partial}{\partial y}\left(\overline{u'v'}\right)+\frac{\partial}{\partial z}\left(\overline{u'w'}\right)\right] \tag{3.10}$$

$$\rho\left[\frac{\partial V}{\partial t}+\frac{\partial}{\partial x}(VU)+\frac{\partial}{\partial y}(VV)+\frac{\partial}{\partial z}(VW)\right]=-\frac{\partial P}{\partial y}+\mu\left(\frac{\partial^2 V}{\partial x^2}+\frac{\partial^2 V}{\partial y^2}+\frac{\partial^2 V}{\partial z^2}\right)$$
$$-\rho\left[\frac{\partial}{\partial x}\left(\overline{v'u'}\right)+\frac{\partial}{\partial y}\left(\overline{v'v'}\right)+\frac{\partial}{\partial z}\left(\overline{v'w'}\right)\right] \tag{3.11}$$

$$\rho\left[\frac{\partial W}{\partial t}+\frac{\partial}{\partial x}(WU)+\frac{\partial}{\partial y}(WV)+\frac{\partial}{\partial z}(WW)\right]=-\frac{\partial P}{\partial z}-\rho g+$$
$$\mu\left(\frac{\partial^2 W}{\partial x^2}+\frac{\partial^2 W}{\partial y^2}+\frac{\partial^2 W}{\partial z^2}\right)-\rho\left[\frac{\partial}{\partial x}\left(\overline{w'u'}\right)+\frac{\partial}{\partial y}\left(\overline{w'v'}\right)+\frac{\partial}{\partial z}\left(\overline{w'w'}\right)\right] \tag{3.12}$$

Taking the Reynolds average gives rise to the Reynolds stress tensor with nine components: $\tau_{xx} = -\overline{u'u'}$, $\tau_{xy} = -\overline{u'v'}$, $\tau_{xz} = -\overline{u'w'}$, $\tau_{yx} = -\overline{v'u'}$, $\tau_{yy} = -\overline{v'v'}$, $\tau_{yz} = -\overline{v'w'}$, $\tau_{zx} = -\overline{w'u'}$, $\tau_{zy} = -\overline{w'v'}$ and $\tau_{zz} = -\overline{w'w'}$. These are six unknown quantities, in addition to the Reynolds-averaged pressure and velocity components: P, U, V and W. To close the system, it is necessary to introduce turbulence closure schemes.

3.1.2 Turbulence closure

Using the Boussinesq approximation, the Reynolds stresses are related to the mean flow strain rates through a turbulent eddy viscosity ν_t as

$$\tau_{xx} = 2\nu_t S_{xx}, \quad \tau_{xy} = 2\nu_t S_{xy}, \quad \tau_{xz} = 2\nu_t S_{xz} \tag{3.13a,b,c}$$

$$\tau_{yx} = 2\nu_t S_{yx}, \quad \tau_{yy} = 2\nu_t S_{yy}, \quad \tau_{yz} = 2\nu_t S_{yz} \tag{3.14a,b,c}$$

$$\tau_{zx} = 2\nu_t S_{zx}, \quad \tau_{zy} = 2\nu_t S_{zy}, \quad \tau_{zz} = 2\nu_t S_{zz}. \tag{3.15a,b,c}$$

The mean flow strain rates are given by

$$S_{xx} = \frac{1}{2}\left(\frac{\partial U}{\partial x} + \frac{\partial U}{\partial x}\right), \; S_{xy} = \frac{1}{2}\left(\frac{\partial U}{\partial y} + \frac{\partial V}{\partial x}\right), \; S_{xz} = \frac{1}{2}\left(\frac{\partial U}{\partial z} + \frac{\partial W}{\partial x}\right) \tag{3.16a,b,c}$$

$$S_{yx} = S_{xy}, \; S_{yy} = \frac{1}{2}\left(\frac{\partial V}{\partial y} + \frac{\partial V}{\partial y}\right), \; S_{yz} = \frac{1}{2}\left(\frac{\partial V}{\partial z} + \frac{\partial W}{\partial x}\right) \tag{3.17a,b,c}$$

$$S_{zx} = S_{xz}, \; S_{zy} = S_{yz}, \; S_{zz} = \frac{1}{2}\left(\frac{\partial W}{\partial z} + \frac{\partial W}{\partial z}\right) \tag{3.18a,b,c}$$

The eddy viscosity is obtained from the k-ω turbulence model.

3.1.3 The k-ω model

Different types of turbulence-closure models have been developed in the past decades, including zero-equation model, one-equation models and two-equation models (Wilcox, 1994). This study uses the k-ω model, which is the first two-equation turbulence model, proposed by Kolmogorov (1942). It is assumed that the turbulence kinetic energy k and the energy dissipation per unit k denoted by ω (i.e. ε/k) are governed by two transport equations.

The development of the transport equations is based on the following reasoning:

- The turbulence kinetic energy k already appears in $\tau_{zy} = 2v_t S_{xy} - \frac{2}{3}k\delta_{xy}$, where the subscripts i and j are standard tensor notations; it is conceivable that $v_t \infty k$.
- The ratio v_t/k has the dimension of time as the dimension of eddy viscosity is m^2/s and the dimension of k is m^2/s^2.
- Turbulence dissipation rate ε has the dimension of m^2/s^3, and consequently ε/k has the dimension of s^{-1}.
- Thus, the system can be closed if $\tau_{xy} = 2v_t S_{xy} - \frac{2}{3}k\delta_{xy}$ and a variable with s or s^{-1} as its dimension is introduced.

Given that the most common processes in fluid motions are unsteadiness, convection, diffusion, dissipation, dispersion and production. Kolmogorov (1942) combined the physical processes with dimensional arguments and proposed a transport equation for ω as

$$\frac{\partial \omega}{\partial t}+\left(U\frac{\partial \omega}{\partial x}+V\frac{\partial \omega}{\partial y}+W\frac{\partial \omega}{\partial z}\right)=-\beta\omega^2 \\ +\left[\frac{\partial}{\partial x}\left(\sigma\nu_t\frac{\partial \omega}{\partial x}\right)+\frac{\partial}{\partial y}\left(\sigma\nu_t\frac{\partial \omega}{\partial y}\right)+\frac{\partial}{\partial z}\left(\sigma\nu_t\frac{\partial \omega}{\partial z}\right)\right] \tag{3.19}$$

where β and ω are two new closure coefficients. The equation is not written in terms of ω^2 as ω^2 is the mean square vorticity of the "energy containing" eddies and k is the kinetic energy of motion induced by the vorticity. A production term was added to the equation later by other researchers.

The k-ω model equations, closure coefficients and relationships used in this study are as follows (Wilcox, 1994):

$$\nu_t=\frac{k}{\tilde{\omega}} \tag{3.20}$$

where, $\tilde{\omega}=\max\left\{\omega, C_{\lim}\sqrt{\frac{2(S_{xx}^2+S_{xy}^2+S_{xz}^2+S_{yx}^2+S_{yy}^2+S_{yz}^2+S_{zx}^2+S_{zy}^2+S_{zz}^2)}{\beta^*}}\right\}$,

C_{lim} =7/8.

$$\frac{\partial k}{\partial t}+U\frac{\partial k}{\partial x}+V\frac{\partial k}{\partial y}+W\frac{\partial k}{\partial z}=P_r-\beta^* k\omega \\ +\frac{\partial}{\partial x}\left[\left(\nu+\sigma^*\frac{k}{\omega}\right)\frac{\partial k}{\partial x}\right]+\frac{\partial}{\partial y}\left[\left(\nu+\sigma^*\frac{k}{\omega}\right)\frac{\partial k}{\partial y}\right]+\frac{\partial}{\partial z}\left[\left(\nu+\sigma^*\frac{k}{\omega}\right)\frac{\partial k}{\partial z}\right] \tag{3.21}$$

$$\frac{\partial \omega}{\partial t}+U\frac{\partial \omega}{\partial x}+V\frac{\partial \omega}{\partial y}+W\frac{\partial \omega}{\partial z}=\alpha\frac{\omega}{k}P_r-\beta\omega^2 \\ +\frac{\partial}{\partial x}\left[\left(\nu+\sigma\frac{k}{\omega}\right)\frac{\partial \omega}{\partial x}\right]+\frac{\partial}{\partial y}\left[\left(\nu+\sigma\frac{k}{\omega}\right)\frac{\partial \omega}{\partial y}\right]+\frac{\partial}{\partial z}\left[\left(\nu+\sigma\frac{k}{\omega}\right)\frac{\partial \omega}{\partial z}\right]+ \\ \left[\left(\frac{\sigma_d}{\omega}\frac{\partial k}{\partial x}\frac{\partial \omega}{\partial x}\right)+\left(\frac{\sigma_d}{\omega}\frac{\partial k}{\partial y}\frac{\partial \omega}{\partial y}\right)+\left(\frac{\sigma_d}{\omega}\frac{\partial k}{\partial z}\frac{\partial \omega}{\partial z}\right)\right] \tag{3.22}$$

where P_r is the production term given by,

$$p_r = 2v_t \left(\begin{array}{l} S_{xx}\frac{\partial U}{\partial x} + S_{xy}\frac{\partial U}{\partial y} + S_{xz}\frac{\partial U}{\partial z} + S_{yx}\frac{\partial V}{\partial x} + S_{yy}\frac{\partial V}{\partial y} + S_{yz}\frac{\partial V}{\partial z} + \\ S_{zx}\frac{\partial W}{\partial x} + S_{zy}\frac{\partial W}{\partial y} + S_{zz}\frac{\partial W}{\partial z} \end{array} \right) \quad (3.23)$$

There are a number of closure coefficients and auxiliary relations, given by

$$\alpha = \frac{13}{25}, \beta = \beta_0 f_\beta, \beta^* = \frac{9}{100}, \sigma = \frac{1}{2}, \sigma^* = \frac{3}{5}, \sigma_{d0} = \frac{1}{8} \quad (3.24)$$

$$\sigma_d = \begin{cases} 0, for \frac{\partial k}{\partial x}\frac{\partial \omega}{\partial x} + \frac{\partial k}{\partial y}\frac{\partial \omega}{\partial y} + \frac{\partial k}{\partial z}\frac{\partial \omega}{\partial z} \le 0 \\ \sigma_{d0}, for \frac{\partial k}{\partial x}\frac{\partial \omega}{\partial x} + \frac{\partial k}{\partial y}\frac{\partial \omega}{\partial y} + \frac{\partial k}{\partial z}\frac{\partial \omega}{\partial z} \succ 0 \end{cases} \quad (3.25)$$

$$\beta = 0.0708, f_\beta = \frac{1+85\chi_\omega}{1+100\chi_\omega}, \chi_\omega \equiv \left| \frac{\Omega_{ij}\Omega_{jk}S_{ki}}{(\beta^*\omega)^3} \right| \quad (3.26)$$

$$\varepsilon = \beta^* \omega k, l = k^{1/2} / \omega \quad (3.27)$$

The two tensors in equation (3.26) are the mean rotation (vorticity) and mean-strain-rate tensors. The cross diffusion term $\frac{\sigma_d}{\omega}\frac{\partial k}{\partial x_j}\frac{\partial \omega}{\partial x_j}$ is added to equation 3.22 to remove the original model's sensitivity of the free stream value of ω and to remove the sensitivity of the imposed boundary condition. This is good for application to wall-bounded flows. The reciprocal of ω is the time scale on which dissipation of turbulence energy occurs. While the actual process of dissipation takes place in the smallest eddies, the rate of dissipation is the transfer rate of turbulence kinetic energy to the smallest eddies. Therefore, the dissipation rate is set by the properties of the large eddies (scale of k and l). Therefore, ω is indirectly associated with the dissipative process.

The k-ω model is advantageous for more accurate near wall treatment in the viscous sub-layer. In wall bounded and low-Reynolds number flows, automatic wall

treatment switches between a low-Reynolds number formulation (i.e. direct resolution of the boundary layer) at low y+ values and a wall function approach at higher y+ values. The k-ω model is suitable for complex boundary layer flows under adverse pressure gradient and separation, which is appropriate to our problem domain (flow around pier with scour hole geometry) features. Also the k-ω model does not need to use an artificial damping function that has major numerical stability concern.

3.1.4 The volume of fluid method

This study deals with free surface flow. The volume of fluid method is used to determine the shape and location of free surface based on the concept of a fractional volume of fluid. A unity value of the volume fraction corresponds to a full element occupied by the fluid and a zero value indicates an empty element containing no fluid. A value of volume fraction between zero and one means that the corresponding element is the surface (partial) element. The equation of the volume of fluid where F is the volume fraction is given by

$$\frac{\partial F}{\partial t} + U\frac{\partial F}{\partial x} + V\frac{\partial F}{\partial y} + W\frac{\partial F}{\partial z} = 0 \qquad (3.28)$$

3.1.5 Boundary conditions

The model domain has external boundaries such as a channel inlet, a channel outlet, pier surface, channel-bed and channel sidewalls. At the inlet, influx of fluid mass and momentum is imposed; the magnitude of the inlet velocity is specified and the direction is taken to be normal to the boundary. The direction constraint requires

that the flow direction is parallel to the boundary surface normal, which is calculated at each element face on the inlet boundary. The turbulence intensity value of 0.05, referred as the ratio of velocity fluctuation (u') and mean velocity (U) and auto-compute turbulence length scale are specified. Turbulence intensity is the estimate of incoming turbulence intensity on the inlet boundary. Typically for flow in complex geometries with high turbulence, it is set between 0.05 and 0.2. The turbulence length scale is a physical quantity that describes the size of large energy-containing eddies in turbulent flow and typically it is calculated as 7% of the characteristic length (width or height of inlet).

At the outlet, a static pressure is specified as

$$P = \rho_w g F_w \left(h_0 - z\right) \tag{3.29}$$

$$F_w = 1 - F_a \tag{3.30}$$

$$F_a = step\left(\left(z - h_0\right)/1[m]\right) \tag{3.31}$$

Where ρ_w is the density of water, chosen as 997kg/m^3; g is the gravitational acceleration, equal to 9.81m/s^2; F_w is the water volume fraction; F_a is the air volume fraction.

At the solid surface of a pier and the channel-bed, a no-slip wall condition is imposed. The no-slip condition sets the velocity of fluid at the boundary as zero (U_w = 0).The flow near the no-slip wall is modelled using the wall function approach; the near wall tangential velocity is related to the wall shear stress by means of a logarithmic relation. The logarithmic relation for the near wall velocity is given by

$$u^+ = \frac{U_t}{u_\tau} = \frac{1}{\kappa}\ln\left(y^+\right) + C \tag{3.32}$$

$$y^+ = \frac{\rho \Delta y u_\tau}{\mu} \tag{3.33}$$

$$u_\tau = \left(\frac{\tau_w}{\rho} \right)^{1/2} \tag{3.34}$$

where u^+ is the near wall velocity, U_t is the known velocity tangent to the wall at a distance of Δy from the wall, u_τ is the frictional velocity, y^+ is the dimensionless distance from the wall, κ is the von Karman constant, and C is the log-log layer constant depending on wall roughness.

On the channel sidewalls and the upper-most air surface boundary, a freely slippery wall condition is applied. In this case, the velocity component parallel to the boundaries has a finite value (which is computed), but the velocity normal to them and the wall shear stress are both set to zero ($Un_w = 0$, $\tau_w = 0$).

3.2 The SPH model

The SPH method has a number of fundamental features. A set of particles possessing individual material properties represent the state of a system. These particles move according to governing conservation equations. Since its development for astrophysical problems (Lucy, 1977; Gingold and Monaghan, 1977), this method has been extensively studied and extended to dynamic fluid flows with large deformations. The key features of the method are summarised below

- The use of the weighted average over the neighbouring particles for stability implies the smoothed approximation nature for hydrodynamics problems.

- The adaptable nature of the method is achieved at a very early stage of the field variable approximation which is performed at each time step based on a current local set of arbitrary distributed particles (Liu and Liu, 2003, page:27).
- The method does not require a pre-defined mesh system to provide any connection within the particles in the process of computation and works efficiently without any particle refinement operation.
- The method is the harmonic combination of the Lagrangian formulation and particle approximation, because particles are not only used as interpolation points but also carry material properties (Liu and Liu, 2003, page:27).
- The method requires no generation of a mesh system for numerical simulations. The generation of a mesh system can be difficult, and the required mathematical transformation of model equations can be more expensive than solving the problem itself.

3.2.1 Theoretical formulation

The SPH formulation is often divided into two key steps. The first step is the integral representation or the so-called kernel approximation of field functions. The concept of integral representation of a function starts from the following identity

$$f(x)=\int_{\Omega} f(x')\delta(x-x')dx' \tag{3.35}$$

where f is a function of the three-dimensional position vector $\vec{x}$ and $\delta(x-x')$ is a Dirac delta function given by

$$\delta(x-x')=\begin{cases}1 & x=x'\\ 0 & x\neq x'\end{cases} \tag{3.36}$$

In equation (3.35), Ω represents the volume integral that contains x. If the Delta function is replaced by a smoothing function $W\left(x-x^{'},h\right)$, than the kernel approximation is given by

$$f(x)=\int_{\Omega} f\left(x^{'}\right)W\left(x-x^{'},h\right)dx^{'} \tag{3.37}$$

where W is the so-called smoothing kernel function (or smoothing kernel or kernel function or simply kernel) and h is the smoothing length defining the influence area of the smoothing function W. The function should satisfy a number of conditions:

- It must be normalised (unity) over the support domain

$$\int_{\Omega} W\left(x-x^{'},h\right)dx^{'}=1 \tag{3.38}$$

- It should be compactly supported

$$W\left(x-x^{'},h\right)dx^{'}=0 \quad when\left|x-x^{'}\right|\succ \kappa h \tag{3.39}$$

- It should be positive, i.e. $W(x-x')\geq 0$, for any point at x' within the support domain of the particle at point x'.
- Its value for a particle should be monotonically decreasing with the increasing distance away from the particle.
- It should satisfy the Dirac delta function property, as the smoothing length approaches to zero

$$\lim_{h\to 0} W\left(x-x^{'},h\right)=\delta\left(x\right|-x^{'}) \tag{3.40}$$

- It should be an even function.
- It needs to be sufficiently smooth.

The second step is the particle approximation. Integral representations can be converted to discretised forms of summation over all the particles in the support domain which is commonly known as particle approximation.

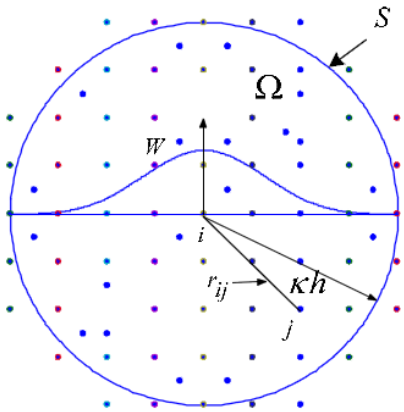

Figure 3.1 Particle approximations using particles within the support domain of the smoothing function W for particle i. The support domain is circular with a radius of κh (Liu and Liu, 2003, page: 41).

3.2.2 Weighting function or smoothing kernel

For numerical simulations using the SPH method, there are four choices of different kernel definitions:

(a) Gaussian function:

$$W(r,h)=\alpha_D \exp\left(-q^2\right) \tag{3.41}$$

where $\alpha_D = 1/\left(\pi h^2\right)$ in 2D and $\alpha_D = 1/\left(\pi^{3/2} h^3\right)$ in 3D.

b) Quadratic function:

$$W(r,h)=\alpha_D\left[\frac{3}{16}q^2-\frac{3}{4}q+\frac{3}{4}\right] \quad 0\le q\le 2 \tag{3.42}$$

where $\alpha_D = 2/\left(\pi h^2\right)$ in 2D and $\alpha_D = 5/\left(4\pi h^3\right)$ in 3D.

c) Cubic spline function:

$$W(r,h)=\begin{cases}1-\frac{3}{2}q^2+\frac{3}{4}q^3 & 0\le q\le 1\\ \frac{1}{4}(2-q)^3 & 1\le q\le 2\\ 0 & q\ge 2\end{cases} \qquad (3.43)$$

where $\alpha_D = 10/(7\pi h^2)$ in 2D and $\alpha_D = 1/(\pi h^3)$ in 3D.

d) Quintic (Wendland, 1995):

$$W(r,h)=\alpha_D\left(1-\frac{q}{2}\right)^4(2q+1) \qquad 0\le q\le 2 \qquad (3.44)$$

where $\alpha_D = 7/(4\pi h^2)$ in 2D and $\alpha_D = 21/(16\pi h^3)$ in 3D.

Choice of kernel function depends on the experience of researchers, though its not unique (Monaghan 1992, Benz 1990, Liu 2003). According to Monaghan (1992), the kernel based on cubic spline function is advantageous as it has compact support feature and the second derivative is continuous.

3.2.3 Governing equations

In SPH, the governing equations for dynamic fluid flows are written as a set of partial differential equations in Lagrangian description, known as the Navier-Stokes equations. These equations are based on the conservation of mass, momentum and energy (Liu and Liu, 2003)

$$\frac{D\rho}{Dt}=-\rho\frac{\partial u^y}{\partial x^y} \qquad (3.45)$$

$$\frac{Du_x}{Dt}=\frac{1}{\rho}\frac{\partial \sigma^{xy}}{\partial x^y} \qquad (3.46)$$

where, *u* is the velocity; *ρ* is the fluid density; σ is the total stress tensor, composed of the isotropic pressure p and viscous stress τ; *e* is the internal energy and x,y denote the coordinate directions. The SPH equations for the Navier-Stokes equations for the conservation of mass and momentum can be written as

$$\frac{D\rho_x}{Dt} = \rho_x \sum_y \frac{m_y}{\rho_y} v_{xy} . \nabla_x W_{xy} \tag{3.47}$$

$$\frac{Du_x}{Dt} = -\sum_y m_y \left(\frac{p_y}{\rho_y^2} + \frac{p_x}{\rho_x^2} \right) \nabla_x W_{xy} - g \tag{3.48}$$

where g is the gravitational acceleration.

3.2.4 Equation of state

To solve the SPH formulation, there must be a relationship between the density of a particle and its pressure. This can be in the form of the Tait state equation (Tait, 1888), the ideal gas equation or Poisson equation. Batchelor (1974) and Monaghan (1992) suggested the following expressions

$$p = B\left[\left(\frac{\rho}{\rho_0} \right)^{\gamma} - 1 \right] \tag{3.49}$$

$$B = \frac{c_0^2 \rho_0}{\gamma} \tag{3.50}$$

$$c_o = c(\rho_o) \tag{3.51}$$

where γ is a constant (= 7); ρ_0 is the reference water density (1000kg/m^3); c_0 is the reference speed of sound in the water. This relation allows for the pressure to be calculated directly from the densities of the fluid particles at each time step in a simplified manner.

3.2.5 Artificial viscosity

The viscosity of the fluid to be modelled is a key parameter in the conservation of momentum. Among different approaches for viscosity, the artificial viscosity proposed by Monaghan (1992) is widely used due to its simplicity. In SPH notation, with the artificial viscosity term Π_{xy} incorporated, the momentum equation can be written as

$$\left(\frac{Du}{Dt}\right)_x = -\sum_y m_y \left(\frac{p_y}{\rho_y^2} + \frac{p_x}{\rho_x^2} + \Pi_{xy}\right) \nabla_x W_{xy} - g \tag{3.52}$$

$$\Pi_{xy} = \begin{cases} \dfrac{-\alpha \overline{c_{xy}} \mu_{xy}}{\overline{\rho_{xy}}} & u_{xy} x_{xy} \prec 0 \\ 0 & u_{xy} x_{xy} \succ 0 \end{cases} \tag{3.53}$$

where $\mu_{xy} = \left(h u_{xy} x_{xy}\right) / \left(r_{xy} + \eta^2\right)$; $u_{xy} = u_x - u_y$; $x_{xy} = x_x - x_y$; the mean speed of sound $\overline{c_{xy}} = \left(c_y + c_x\right)/2$. The parameter $\eta^2 = 0.01 h^2$ is included to avoid singularities. The parameter α is a free parameter depending on the problem domain.

3.2.6 Particle motions

Particles move in the model domain using the XSPH variant due to Monaghan (1989); particles move with a velocity that is close to the average velocity of its neighbourhood.

$$\frac{dx_x}{dt} = u_x + \varepsilon \sum_y \frac{m_y}{\overline{\rho_{xy}}} u_{xy} W_{xy} \tag{3.54}$$

where $0 \le \varepsilon \le 1$ is a constant and $\overline{\rho}_{xy} = \left(\rho_y + \rho_x\right)/2$ is the mean density.

3.2.7 Time stepping

SPH simulations can be performed through time using four different time-stepping algorithms.

(a) The predictor-corrector scheme proposed by Monaghan (1989), which works in such a way that the velocity, density, position and energy are first, calculated at every time step and corrected with the forces at half-time step.

(b) The time stepping theorem by Verlet (1967), which uses two sets of equations based on a third-order Taylor expansion series, where variables are evaluated at each time step.

(c) The Beeman scheme, which uses a Beeman predictor step and an Adams-Bashforth-Moulton corrector step.

(d) The symplectic algorithm proposed by Leimkhuler (1997), is time reversible in the absence of friction or viscous effects and hence represents a very attractive option for mesh-free particle schemes.

Time step control depends on the Courant number (or the CFL condition), forcing terms and viscous term (Monaghan, 1989). According to Monaghan and Kos (1999), time step can be calculated from (SPHysics Guide v2.0.001, 2010)

$$\Delta t = 0.3 \min\left(\Delta t_f, \Delta t_{cv}\right) \tag{3.55}$$

$$\Delta t_f = \min_x \sqrt{h/|f_x|} \tag{3.56}$$

$$\Delta t_{cv} = \min_x \frac{h}{c_s + \max_y \left| h_{xy} r_{xy} / r_{xy}^2 \right|} \tag{3.57}$$

where Δt_f is based on the force per unit mass f_x; Δt_{cv} combines the Courant and viscous time step controls; f_x corresponds to all forces exerted on particle x.

The DualSPHysics code has only choice between Verlet and Symplectic algorithms as time integration schemes. According to Gomez-Gesteira *et al.* (2010) it is advantageous to use at least a second order accurate scheme in time since the particle are moving in space. The Verlet time stepping algorithm has been used in our simulation for this reason.

3.2.8 Boundary conditions

The boundary conditions do not appear in a natural way in the SPH formulation. The numerical model must take place inside a specific region of particles that exhibit special characteristics. When a fluid particle approaches a solid boundary, only the particles located inside the domain are included in the SPH interpolation without any interaction from outside.

Several types of virtual particles, which characterize the limits of the domain, need to be created. One of the techniques is imposing dynamic boundary conditions which make these particles to follow the same continuity equation and equation of state as done by fluid particles. However, these particles do not move according to momentum equation and remain fixed in position (fixed boundaries) or move according to some externally imposed function (moving objects like gates, wavemakers).

Another boundary condition is repulsive boundary conditions developed by Monaghan (1994) to ensure that a fluid particle can never cross solid boundary. The

boundary particles exert central forces on the fluid particles. This method was modified by Monaghan and Kos (1999) imposing an interpolation process, minimizing the inter-spacing effect of the boundary particles on the repulsion force of the wall.

Open boundaries are implemented using periodic boundary conditions which means that the particles near an open lateral boundary interact with the particles near the complementary open lateral boundary on the other side of the domain.

3.2.9 Computational efficiency: linked lists

The computational domain is divided into square cells of side *nh* following Monaghan and Lattanzio (1985) where *n* depends on the particular choice of the kernel. Thus for a particle located inside cell, only the interactions with the particles of neighboring cells need to be considered. In this way the number of calculations per time step diminishes from N^2 operations to the order of N, N being the number of particles (SPHysics Guide v2.0.001, 2010). This considerably saves computational time.

In summary, SPHysics is a platform of SPH codes inspired by the formulation of Monaghan (1992) developed jointly by researchers at the John Hopkins University, the University of Vigo, the University of Manchester and the University of Rome La Sapienza. A community approach was adopted to develop the model. The serial model has been written in Fortran 90. To create more efficient executable files different modules can be included or excluded and only relevant algorithms are compiled. The serial model has been constantly in evolution since the first release in 2007 until its eighth update in January 2011. To execute parallel and

supercomputers, a parallel version of the code parallel-SPHysics has been released in 2011. The latest version named DualSPHysics released on March 2012 has been designed to be run on either multicore Central Processing Units (CPUs) or Graphics Processing Units (GPUs).

The serial code of SPHysics written in FORTRAN 90 language can simulate free surface flow scenarios in both two- (2D) and three-dimensions (3D). The model allows introducing obstacles such as trapezoidal or rectangular structures at any location of the problem domain. Slope of the bottom geometry can be added to model beach-type geometry. Waves can be generated using paddle or piston type wave makers.

To solve the problem for the application of SPHysics to real-life engineering problems in long computational time, the use of Graphics Processing Units (GPUs) appears as a cheap alternative high performance computing for numerical computing. Compute Unified Device Architecture (CUDA) is a parallel programming framework and language for GPU computing using some extensions to the C/C++ language. DualSPHysics, also known as GPUSPH is implemented in C++ and CUDA language to carry out simulations on the CPU and GPU respectively. The new CPU code is advantageous in case of optimum use of memory. Implementation of parallelize particle interaction on GPU was first done by Crespo *et al.* (2009). Another major improvement in GPUSPH is the provision of using external complex geometries. This helps to create real time bathymetry in open channel flow (Crespo *et al.* 2011, Gomez-Gesteira *et al.* 2012a, 2012b).

Chapter Four Model Setup

4.1 Model channel and setup of FEM simulations

The model channel considered in the research is illustrated in Figure 4.1 in the Cartesian coordinates (x, y, z). The pier has a diameter of D = 15 cm. The red line marks the equilibrium position of the free water surface. Above this surface, there is a layer of air 0.33D thick. The fixed scour hole around the pier has the same bottom profile along the channel centerline as Graf and Istiarto's (2002) experimental channel. The model channel has a width of 7.67D on both sides of pier, and a length of 6D and 14.33D, respectively, upstream and downstream of the pier. The equilibrium water depth outside the scour hole is h_o = 1.2D. Water flow approaches the scour hole from the positive direction of the *x*-axis or from left to right.

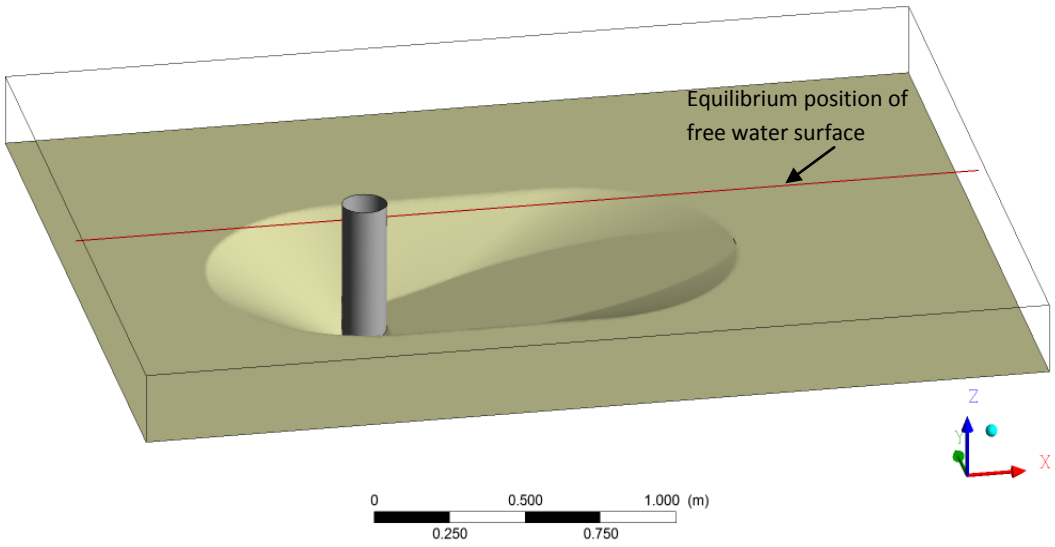

Figure 4.1 A three-dimensional view of the model channel used in mesh-based FEM simulations.

Table 4.1 A summary of control parameters and variables used in FEM simulations.

Parameter / variable	Value	Unit
Time step (Δt)	0.01	s
Simulation duration	15	s
Pier diameter (D)	0.15	m
Channel length upstream of the pier (L_1)	0.975	m
Channel length downstream of the pier (L_2)	2.075	m
Channel width on both sides of the pier (B)	1.15	m
Discharge (Q)	0.2	m^3/s
Initial water depth outside the scour hole (h_o)	0.18	m
Initial thickness of the air layer	0.05	m
Inclination of the scour hole upstream of the pier	29	deg
Inclination of the scour hole downstream of the pier	10	deg
Scour hole length upstream and downstream of the pier	0.45, 1.2	m

The hydraulic conditions and channel geometry used in FEM simulations (Table 4.1) match the experiment setup of Graf and Istiarto (2002). This allows a direct comparison between the results from this modelling research and the laboratory measurements of Graf and Istiarto (2002). A comparison will be made of vertical profiles of predicted longitudinal velocity with available measured velocity profiles at 14 locations, labelled as f1 to f7 and b1 to b7 in Figure 4.2. In addition, a comparison of predicted and measured bed shear stresses distributed along the channel centreline will be presented.

The approach flow has a depth-averaged velocity of u_o = 0.45 m/s. The Froude number is calculated to be 0.34, based on h_o and u_o. A two-phase flow problem was considered, where air at 25^{o}c and water are defined as model fluids, each being treated as a homogeneous continuous fluid. The interface between air and water or the free-water surface is specified as that the fluid particles on the surface remain there all the time. There is no mass transfer across the interface. Reference pressure is set at 1 atm with gravity acting in the negative z-direction.

Heat transfer is fixed as isothermal at 25^{o}C temperature with air density of 1.185 kg/m^{3}. The Reynolds number based on the approach flow is 81000.

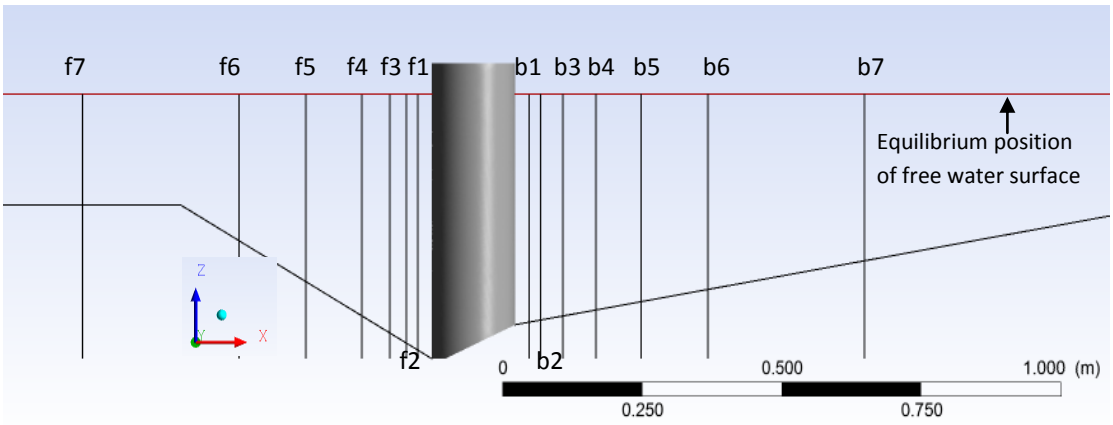

Figure 4.2 The vertical cross section through the model channel centreline, showing the bed-surface profile and 14 locations (f1 to f7 upstrem of the pier and b1 to b7 downstream) from which laboratory measurments of flow velocity (Graf and Istiarto, 2002) are available for verification of FEM predictions.

4.2 Model channel in SPH simulations

The model domain (Figure 4.3) used in mesh-free DualSPHysics simulations consists of an upstream headwater reservoir, a main channel that is similar to that used in the mesh-based FEM simulations, a channel extension downstream of the main channel and a downstream basin. This upstream reservoir has a height of 9 m, a length of 9 m and a width matching that of the main channel. The effects of dimensions chosen for the reservoir on the flow in the channel will be discussed in Chapter Five. A vertical gate, which can be lift in the vertical by up to 0.4 m, is placed between the upstream reservoir and the main channel. This gate controls water flow from the reservoir through the main channel to the downstream basin.

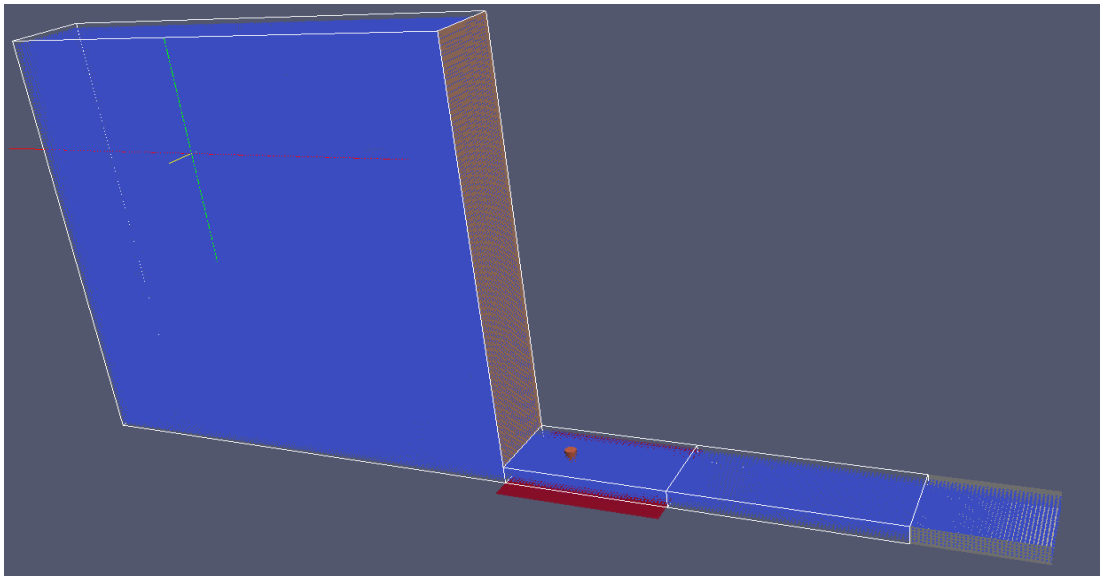

Figure 4.3. A three-dimensinal view of the model domain used in SPH simulations, showing a headwater reservoir, a main channel (Figure 4.4), an auxiliary channel extension downstreanm of the main chanel and a downstream reservoir.

The main channel (Figure 4.4) contains a fixed scour hole whose shape and size are the same as Graf and Istiarto's (2002) laboratory channel, although its width is made smaller than that of the laboratory channel. The width is reduced from 7.67D in the laboratory model to 5D in the SPH model on both sides of the pier. This is to reduce the total fluid volume in the main channel and hence lower the total number of particles needed to adequately represent the fluid volume. Through a series of sensitivity simulations, the effects of width reduction on SPH solutions will be analysed later in Chapter Five. The sensitivity simulations help finalise the main channel, being 3.05 m long and 1.65 m wide, with a scour hole and pier symmetric about the channel centreline.

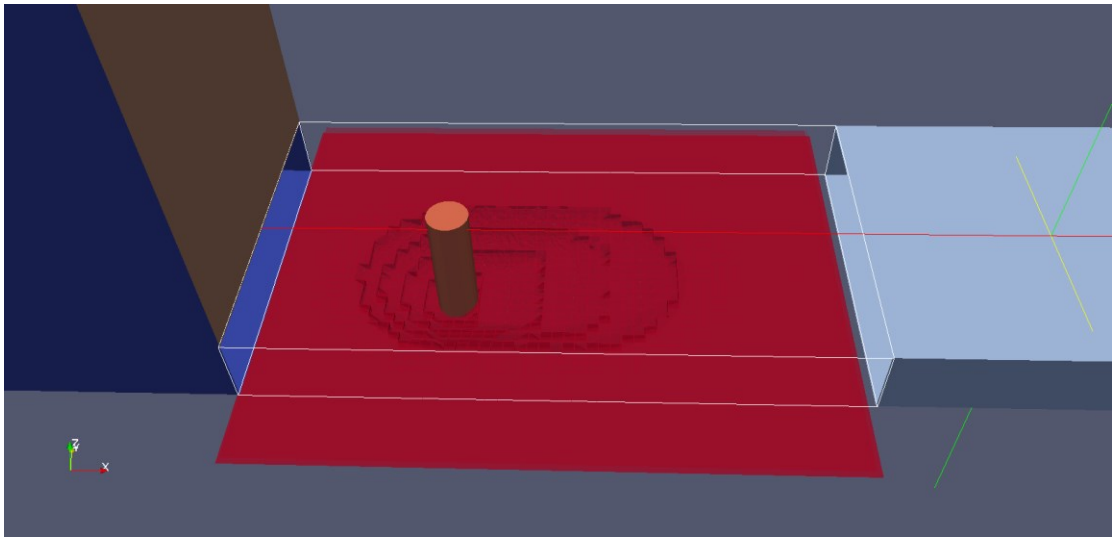

Figure 4.4 Close-up of the main channel (Figure 4.3), showing details of the scour hole with a pier standing in the vertivcal.

In the process of setting up SPH simulations, the initial condition of a dry main channel was considered. In other words, the fluid exits the reservoir like a dam break and enters the main channel as free-surface flow (Figure 4.4). Without a lid over the water surface, it was difficult to control the water level in the main channel and to achieve the target flow depth of 0.18 m as in Graf & Istiarto's (2002) experiment. An adjustment of the fluid volume in the reservoir was found to help achieve the target flow depth, but was not able to produce, at the same time, an inflow velocity below the gate (or approach flow velocity) matching the experimental value of 0.45 m/s. In order to match the experimental values for approach flow depth as well as velocity, the water level was adjusted in the reservoir and introduced a horizontal lid on the top of the main channel.

Test simulations with a lid on the top of the main channel produced vertical profiles of longitudinal velocity, which resemble closed-conduit flow rather than

open-channel flow (Figure 4.5). The main feature is that the longitudinal velocity, U, increases with height, z, from the channel-bed, reaches a peak value at a certain height and decreases further up toward the lid. To deal with this issue, a lid was placed at a height of 0.4 m. The idea is to produce a flow depth of 0.18 m between the channel-bed and the peak velocity height, and at the same time, this portion of the flow has the target depth-averaged velocity of 0.45 m/s. This treatment is acceptable for two simple reasons. First, the shear stress is zero at the peak velocity height, which dynamically resembles open-channel flow. Second, the free-water surface is not far from horizontal over the short length of the main channel. The use of 0.4 m, instead of 0.36 m (corresponding to an exact symmetry of 0.18 m for flow depth), is due to the loss of a thin layer of flow or streamlines near a solid boundary in SPH simulations.

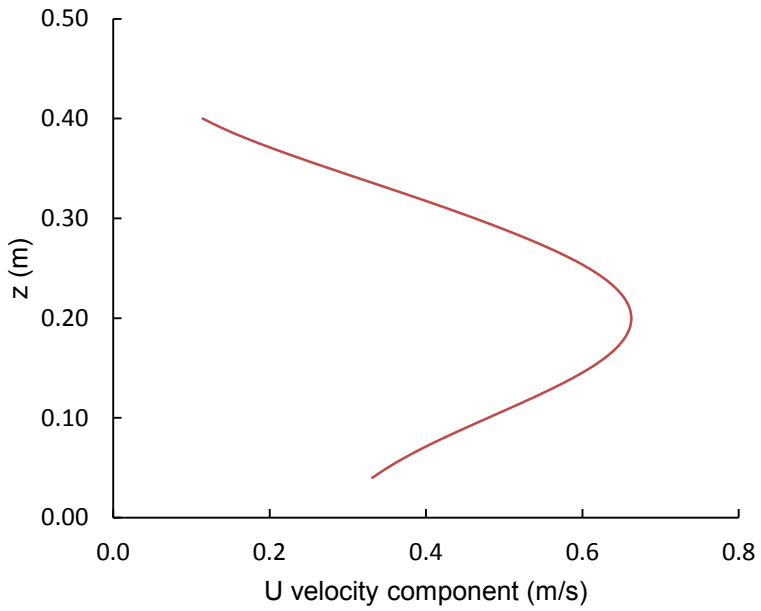

Figure 4.5 Typical vertical profile of longitudinal velocity.

4.3 Time stepping in SPH simulations

The appropriate time duration for SPH simulations is estimated as follows: Initially, when water exits the upstream reservoir (Figures 4.3 and 4.4), the flow below the gate has a velocity of 0.45 m/s. Between the gate and the downstream end of the main channel, the horizontal distance is 3.05 m. Thus, flowing fluid particles will take 6.78 s to cover the distance. This value may be used as a reference value for the time duration to reach a steady state. The number of time steps corresponding to the time duration may be determined by dividing the duration by a chosen time step, Δt, for simulations.

This study uses the cubic spline kernel (Monaghan and Lattanzio, 1985) as the smoothing kernel function. As proposed by Monaghan (2000), the tensile instability correction is applied to avoid particle clumping in this particular cubic spline kernel. The Verlet algorithm is selected as the time-step algorithm with 40 steps to apply the Eulerian equations. Simulations use 6.27s as the model time duration or last 209 time steps with a time step of 0.03 s. As will be illustrated later in Chapter Five, the flow reaches a steady state after 100 time steps (or 3 s of model time) and therefore, the use of a total of more than 200 time steps is adequate to produce steady state flow field. The chosen time step of 0.03 s is small enough to avoid possible numerical noise or fluctuations in numerical solution from one time step to the next. A time series will be extracted of flow velocity at a number of selected locations from SPH results and examine them with respect to equilibrium and noise.

To maintain the approach flow at the desired velocity of 0.45 m/s over the entire simulation duration with a time step of 0.03 s, it is preferred to have a very small distance between fluid particles (*dx*, *dy* and *dz*) in the so-called numerical

upstream reservoir and main channel. However, a decrease in the distance will lead to an increase in the total number of particles needed to fill up the numerical reservoir and channel. To optimise between the requirement and computational costs, the distance between fluid particles was chosen to be $dx = dy = dz = 0.04$ m. A summary of SPH parameters and variables is given in Table 4.2.

Table 4.2 A summary of control parameters and variables used in SPH simulations.

Parameter / variable	Value	Unit
Time step (Δt)	0.03	s
Pier diameter (D)	0.15	m
Reservoir length, width and height	9.0, 1.65, 9.0	m
Main channel length upstream of the pier (L_1)	0.975	m
Main channel length downstream of the pier (L_2)	2.075	m
Main channel width on both sides of the pier (B)	0.825	m
Vertical opening of the reservoir gate	0.40	m
Inclination of the scour hole upstream of the pier	29	deg
Inclination of the scour hole downstream of the pier	10	deg
Scour hole length upstream of the pier	0.45	m
Scour hole length downstream of the pier	1.2	m
Time step algorithm	Verlet	
Verlet Steps (number of steps to apply Eulerian equations)	40	
Kernel selection	cubic spline	
Viscosity formulation	artificial	
Viscosity value	0.25	

Chapter Five Results

5.1 The FEM Model

5.1.1 Sensitivity test and equilibrium solution

For the hydraulic conditions and channel geometry given in Table 4.1, a series of test simulations were carried out to test the independence of numerical solutions to the model equations [equations (3.5) and (3.10)-(3.12)] on mesh configuration in terms of spatial resolution, mesh type and mesh inflation near a solid surface. The basic idea is to progressively refine the mesh on which simulations are performed until the simulated flow field is no longer sensitive to further refinement. The results from different test simulations have been compared quantitatively. When making mesh refinement, a special attention was paid to the scour hole region around the pier as this region is the focus of the present modelling research.

Table 5.1 Quantitative Comparison of flow velocities with different mesh resolutions.

Location	Velocity Components	R1	R2	R3
(0.2,0.5,0.1)	u	0.52	0.5	0.51
	v	0.014	-0.01	-0.01
	w	-0.044	-0.09	-0.095
(0.7,1.0,-0.05)	u	0.36	0.34	0.34
	v	0.007	-0.03	-0.01
	w	-0.105	-0.09	-0.094
(1.2,1.5,0.05)	u	0.33	0.3	0.32
	v	-0.021	-0.01	-0.039
	w	-0.003	-0.0009	0.002
(2.5,2.0,0.15)	u	0.44	0.4	0.44
	v	-0.004	-0.03	-0.02
	w	0.004	0.099	0.042

As an example of quantitative comparison, the predicted flow velocities (in m/s) at four locations: (x, y, z) = (0.2, 0.5, 0.1), (0.7, 1.0, -0.05), (1.2, 1.5, 0.05) and (2.5, 2.0, 0.15), for three simulations (R1, R2 and R3) with different mesh resolutions are shown in Table 5.1. Clearly, all the simulations produce consistent results.

All the test simulations commence from a state of rest or from velocity (U, V, W) = (0, 0, 0) everywhere in the model domain (Figure 4.1); the unsteady model equations [equations (3.5) and (3.10)-(3.12)] are integrated over time for a prescribed time duration (15 second, see Table 4.1). The time duration is chosen to be sufficiently long to ensure that the numerical solution to the model equations reaches a state of equilibrium. The time duration was determined that was needed to reach an equilibrium as follows: First, estimate the advection time as the ratio of the total length of the model channel ($L_1 + L_2$ = 3.05 m, see Figure 4.1 and Table 4.1) to the average flow velocity in the approach channel (0.45 m/s). Then, multiply the advection time by a factor of 2.5 to obtain the simulation time duration (= 15 s, Table 4.1).

An examination of the results (not shown) of equilibrium flow velocity and water surface elevation for the test simulations lead to the ultimate choice of a mesh system for use in subsequent simulations. The use of different mesh types, including tetrahedron, prism, pyramid and hexahedron, was found to have little influence on the results. A tetrahedron-type mesh was used in subsequent simulations. Mesh inflation at solid boundaries (such as the channel-bed and pier surface) is applied in order to effectively resolve near-boundary flow. The use of a mesh system with inflation has produced more realistic flow features.

In FEM, mesh adaptation is available. This is a built-in feature in which the mesh in selected areas is refined with specified control criteria. The purpose of this feature is to accelerate solution convergence at any time step during a simulation, which must not be confused with the idea of testing the independence of solutions to mesh configuration. The mesh can be automatically adjusted at a selected time of simulation at locations where a defined solution variable is varying rapidly. Refining mesh at those points help resolve the flow features better. Mesh adaptation for different solution variables were tested. Applying mesh adaptation after 100 iterations for solutions of the volume of fraction of water was selected. It is appropriate for the multiphase flow simulation performed in our case based on the test simulations.

The sensitivity of solutions to turbulence closure schemes and related parameters was also tested. In general, different turbulence closure schemes have advantages and disadvantages, as discussed in Wilcox (1994). The *k*-ω model is appropriate for the specific application in this research, where the near-boundary flow with complex geometry is adequately resolved.

In summary, the selections of mesh configuration and control parameters through the test simulations mentioned above result in the appropriate determination of the ultimate mesh system. An examination of the model results (not shown) from these test simulations indicates that the model has been set up properly. The model results presented below are equilibrium solutions.

5.1.2 Velocity vector field in the horizontal

In Figure 5.1, velocity vectors at a depth of 0.09 m or 0.6D below the free surface are plotted. Upstream of the pier, water flows around the pier. The presence of the pier in the flow path results in velocity vectors different from location to location in both magnitude and direction, and gives rise to strong clockwise and counter-clockwise circulations just downstream of the pier or wake vortices. Flow separation from the pier surface is visible. The longitudinal or x-component of velocity ranges from -0.33 to 0.63 m/s (compared to the approach flow velocity of u_o = 0.45 m/s). The negative values are associated with wake vortices. The transverse or y-component of flow velocity ranges from -0.26 to 0.32 m/s. The influence of the pier on the flow field diminishes far downstream, where velocity vectors regain uniformity (not shown).

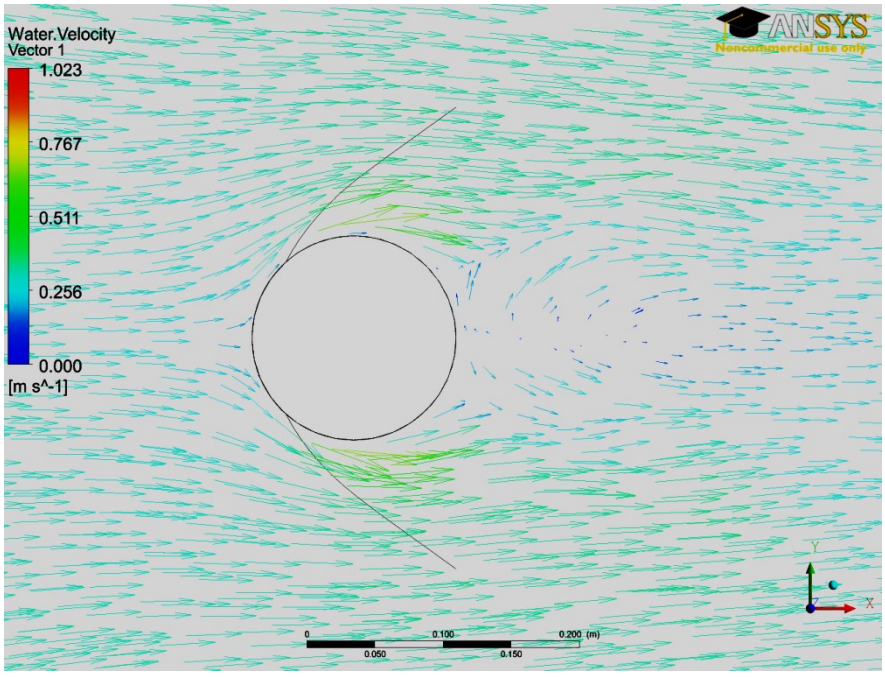

Figure 5.1 A horizontal plane showing velocity vectors at a depth of 0.09 m below the free surface.

Velocity vectors in the scour hole at about half the maximum scour depth are shown in Figure 5.2. The flow shows divergent patterns near the upstream edge of the scour hole. Associated with the divergence is an upward flow from below (not shown). Downstream of the pier, there are virtually no eddy motions and no flow reversal at this specific depth.

No flow separation is visible. Presumably, this is because the flow accelerates under the influence of the rising channel-bed downstream of the pier, which creates a favorable pressure gradient. The longitudinal and transverse (or x and y) components of flow velocity range from -0.14 to 0.54 m/s and from -0.26 to 0.32 m/s, respectively. As expected, the flow velocities inside the scour hole have smaller magnitudes than those above the scour hole shown in Figure 5.1.

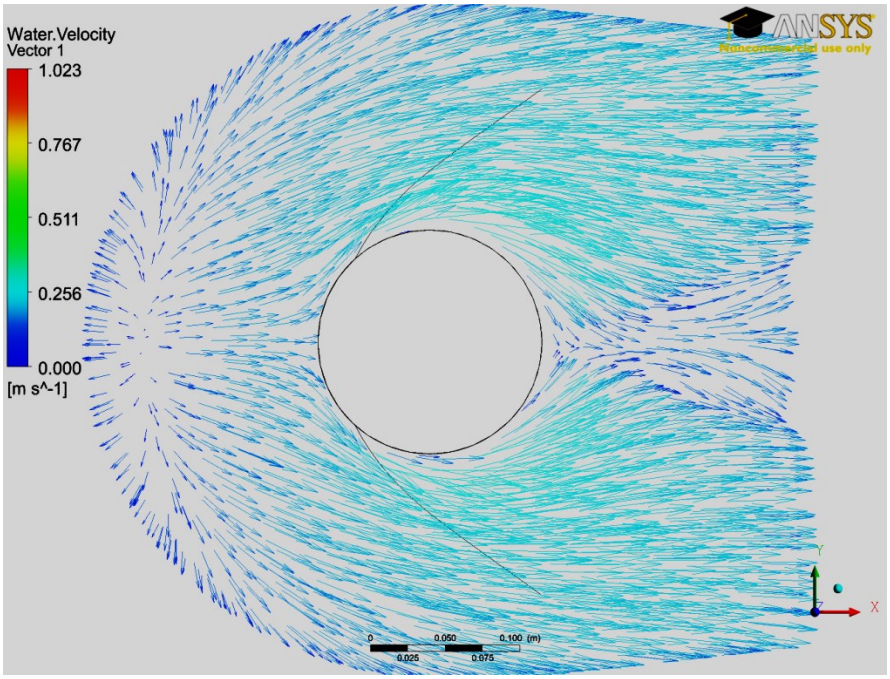

Figure 5.2 A horizontal plane showing velocity vectors inside the scour hole at a depth of 0.35 m below the water surface.

5.1.3 Flow streamlines

Vortex motions around the pier are clearly shown as streamlines in Figure 5.3. A number of observations can be made: (a) the streamlines wrap around the upstream half of the pier at all depths between the free surface and the channel-bed; (b) the streamlines wrap around the entire pier surface over the lower half of the pier, where there is no significant flow separation; (c) from the free surface down to about one third of the pier diameter and downstream of the pier, the streamlines detach from the pier surface, meaning that flow separation takes place there; (d) at a short distance (0.47 to 0.8D) below the free surface, vortex stretching occurs. The implications are that it would be extremely difficult to measure the complex flow features and vortex motions in laboratory experiments.

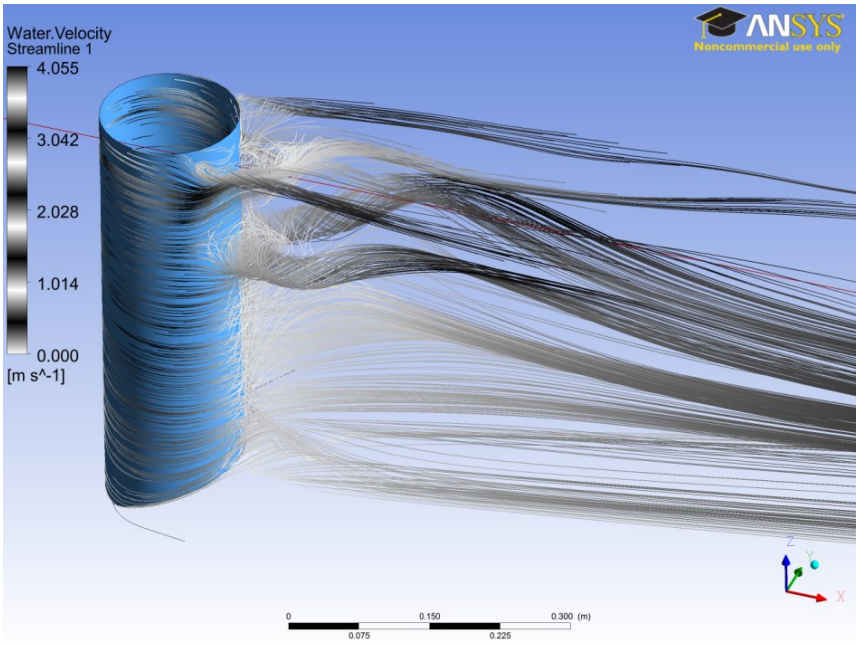

Figure 5.3 Streamlines around the pier, showing flow separation downstream of the pier near free surface and vortex stretching at a short distance below free surface.

5.1.4 Velocity structures in the vertical direction

As illustrated in Figure 5.4, the flow field in the scour hole region is very elaborate. Water enters the scour hole as a jet hugging the bed, with a core of high speed (≈ $1.5u_{o,}$ where u_o is the approach flow velocity equal to 0.45 m/s). Further into the scour hole, eddy motions are visible immediately above the sloping bed. Close to the pier, water flow is deflected downward. Both the eddy motions and downward flow have important implications for the movement of bed sediments. Downstream of the pier, the flow is weak, compared to the condition upstream of the pier, but the flow patterns are much more complicated. This is particularly the case immediately downstream of the pier; the flow is mainly upward.

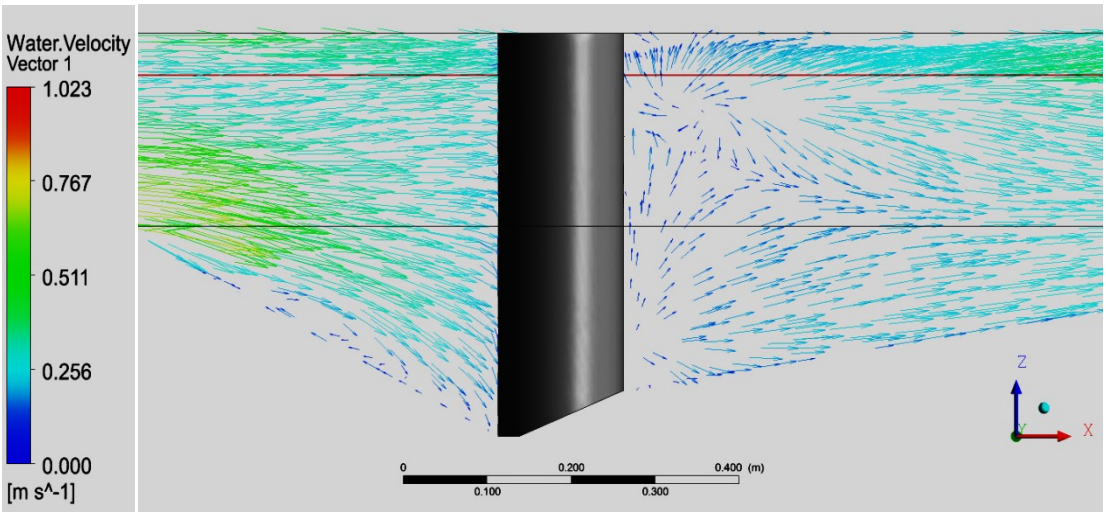

Figure 5.4 Velocity vectors in the plane through the channel centreline. The vectors above the red line are air velocities, where the water volume fraction is zero. The approach flow velocity is u_o = 0.45 m/s.

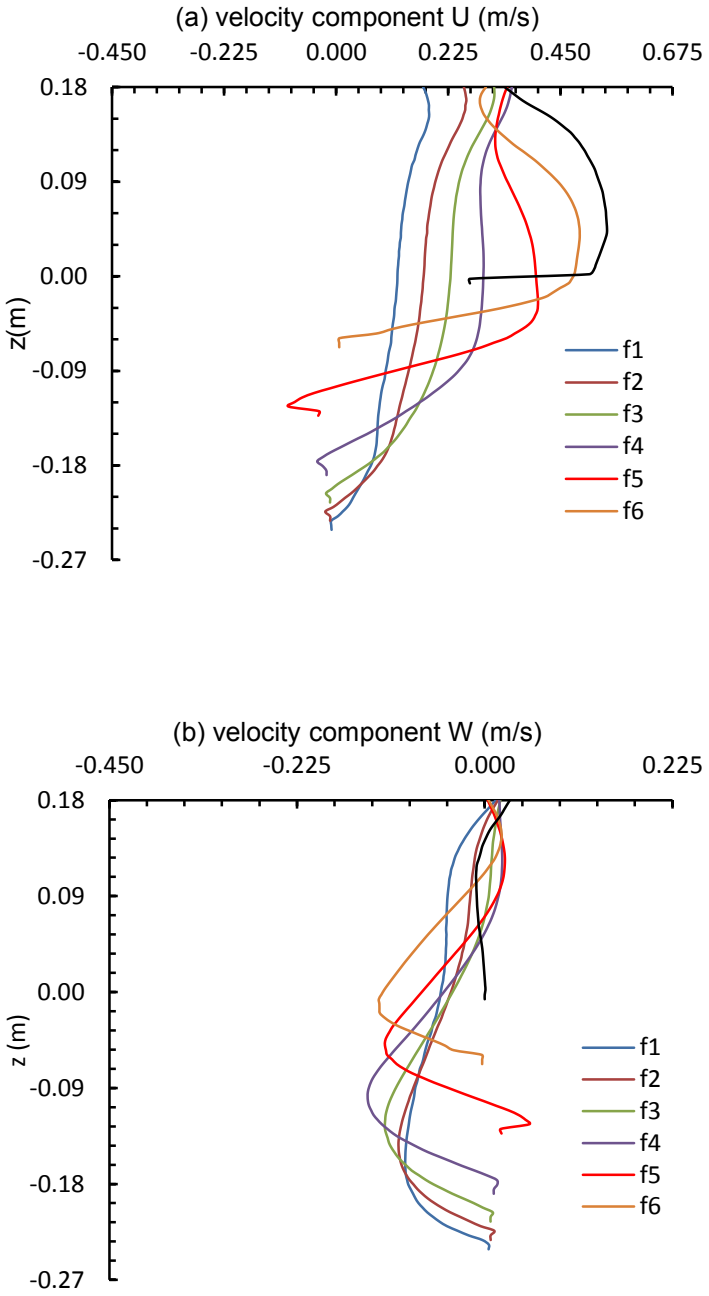

Figure 5.5 Vertical profiles of the longintudinal or x-component and the vertical or z-component of flow velocity at 7 selected locations (labeled as f1 to f7 in Figure 4.2) upstream of the pier.

For a further examination of the vertical structures of the flow, vertical profiles of the longitudinal or x-component of flow velocity at seven locations (f1 to

f7, Figure 4.2) upstream of the pier are plotted in Figure 5.5a. Note that locations f1 to f6 are inside the scour hole and location f7 is outside. The velocity decreases as the flow approaches the pier; the peak velocity is slightly larger than u_o at location f7, and decreases to $0.8u_o$ at location f5 and to less than $0.4u_o$ at location f1. The decrease is due to the pier in the flow path and water column deepening toward the pier. The profile at location f5 shows the most profound vertical structure, with flow reversal near the bed. Inside the scour hole, all the profiles (Figure 5.5b) show significant negative W values or downward velocities. The downward velocity at location f4 is the strongest ($\approx 0.3u_o$). The downward velocities intensify with depth, reach a maximum at a depth in the lower water column, and then weaken toward the bed.

Downstream of the pier, the longitudinal velocities (Figure 5.6a) are mostly positive except in the proximity of the pier (at locations b1 and b2, Figure 4.2). In general, the velocities increase with distance toward downstream, which is particularly the case near the free surface; the increase in velocity near the bed occurs probably because the flow accelerates over the rising bed. Another feature of the profiles is that the individual profiles show an increase in longitudinal velocity with depth below 0.1 m or 0.67D. With respect to the vertical velocity W (Figure 5.6b), it is upward at the free surface. At a depth of about 0.67D, W is upward in the proximity of the pier (at locations b1 and b2) but downward at short distances from the pier (locations b3 to b6).

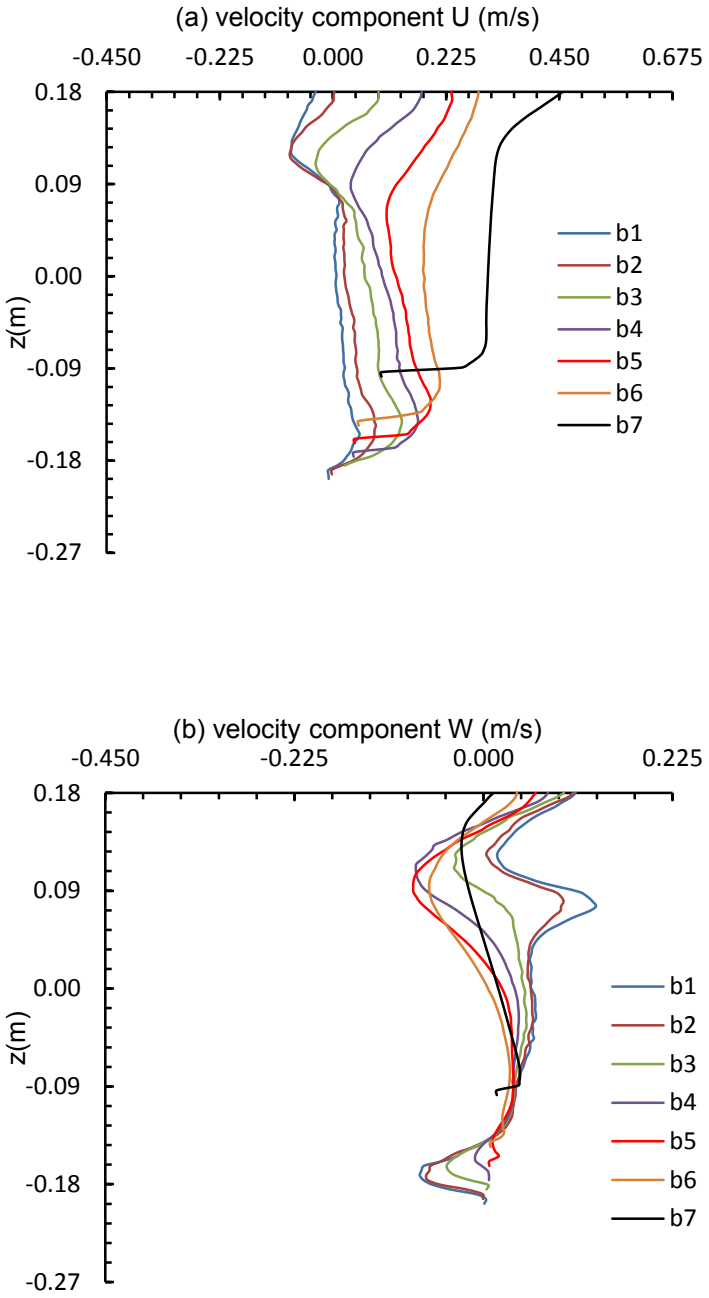

Figure 5.6 Vertical profiles of the x-component and z-component of flow velocity at 7 selected locations (labeled as b1 to b7 in Figure 4.2) downstream of the pier.

5.1.5 Vorticity

Vorticity measures the tendency to form vortices or the local spinning motion of a fluid near some point. Mathematically, the vorticity vector is defined as the curl of the velocity vector field in three dimensions (U, V, W). In Cartesian coordinates, the three components of the vorticity vector are given by

$$\omega_z = \frac{\partial V}{\partial x} - \frac{\partial U}{\partial y} \tag{5.1}$$

$$\omega_y = \frac{\partial U}{\partial z} - \frac{\partial W}{\partial x} \tag{5.2}$$

$$\omega_x = \frac{\partial W}{\partial y} - \frac{\partial V}{\partial z} \tag{5.3}$$

In bridge hydraulics applications, the vorticity vector field associated with the near-bed velocity within the scour hole is the most interesting.

Contours of the vorticity components in the vicinity of the channel-bed are plotted in Figures 5.7a-c. In the xy-plane (Figure 5.7a), the vertical component of the vorticity vector [equation (5.1)] is relatively strong ($\approx \pm 75$ s^{-1}) in small neighbourhoods along the outer edge of the scour hole; the values are positive to the left of the pier (to an observers facing downstream), meaning that fluid particles have the tendency to rotate counter-clockwise about the z-axis (Figure 4.1), as seen from the top by an observer located in the neighbourhoods and travelling along with the fluid; the values are negative to the right of the pier, meaning that fluid particles there have the tendency to rotate clockwise. Relatively strong vorticity is also seen near the upstream nose of the pier, where the fluid is forced to flow around (Figures 5.1 and 5.2). The vertical component of the vorticity appears to be weak in the wake region downstream of the pier.

In the xz-plane (Figure 5.7b) for the y-component of the vorticity vector [equation (5.2)], there is a core area of strong vorticity located in the middle of the upstream portion of the scour hole, with significant implications of sediment scouring. Since the vorticity component has negative values within the core, fluid particles there have the tendency to rotate clockwise, as seen by an observer facing in the positive direction of the y-axis (Figure 4.1). The maximum intensity (≈ 100 s^{-1}) is somewhat higher than that shown in Figure 5.7a. The vorticity is weak outside the core area (Figure 5.7b). Just behind the pier on the downstream side, the tendency to rotate around the y-axis (Figure 4.1) is evident in a very small neighbourhood. Strong vorticity is observed over a very small region at the upstream and downstream edges of the scour hole.

In the yz-plane (Figure 5.7c), the x-component of the vorticity vector [equation (5.3)] is stronger outside the scour hole than inside. The x-component of the vorticity has positive values to the right of the pier (to an observer facing downstream), meaning that fluid particles have the tendency to rotate counter-clockwise, as seen by an observer facing in the positive direction of the x-axis; the values are negative to the left of the pier, meaning that fluid particles there have the tendency to rotate clockwise. Strong vorticity is also observed near the upstream and downstream nose of the pier as the fluid is forced to flow around the pier.

(a) xy-plane

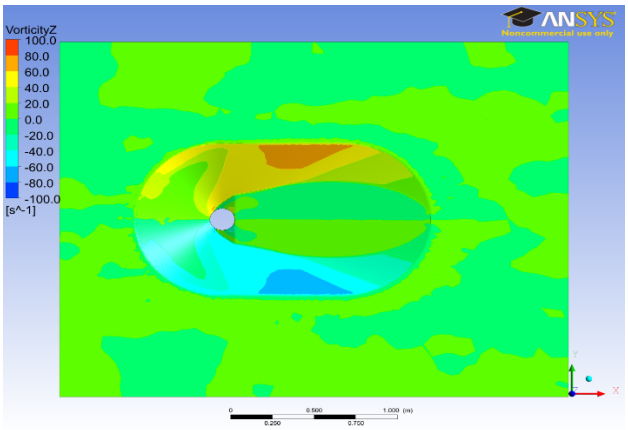

(b) xz-plane

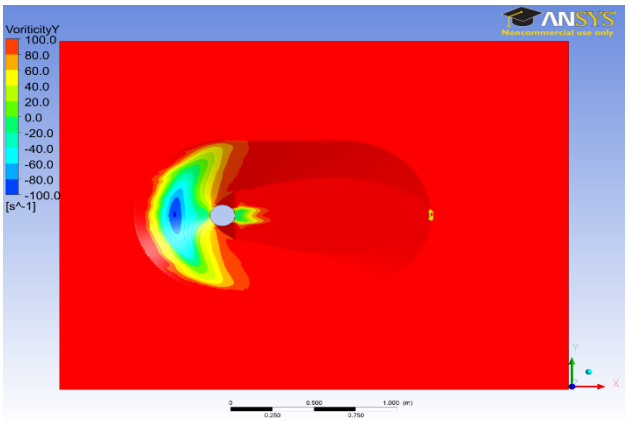

(c) yz-plane

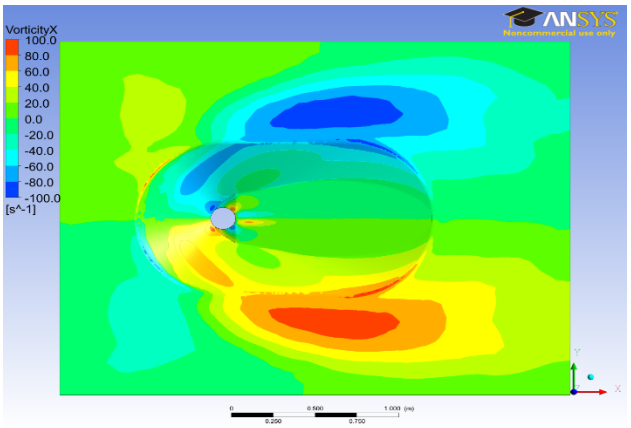

Figure 5.7 Contours of vorticity associated with the near-bed flow velocity: (a) the xy-plane, (b) the xz-plane, and (c) the yz-plane.

5.1.6 Turbulence intensity and bed shear stress

The bed shear stress, τ_b, is an important quantity to predict in studies of scour development. As shown in Figure 5.8, the predicted τ_b values from this study compare reasonably well with experimental data of Graf and Istiarto (2002). There are some discrepancies for the area just before water enters the scour hole; the predictions show a high shear stress peak, which is not seen in the experimental data. A possible explanation is that the local mesh in the vicinity of the channel-bed are not fine enough to adequately resolve the vertical structure of the near-bed flow; it is noticed that the velocity profile shown in Figure 5.5a at location f7 (The located is labeled in Figure 4.2) appears to have an unrealistic shape near the bed. Using the eddy viscosity method $\tau_b = \rho v_t \partial v_{par}/\partial n$, Graf and Istiarto (2002) determined the bed shear stress from laboratory measurements of flow velocity, where v_{par} is a velocity parallel to the bed based on longitudinal and vertical components of flow velocity, n is the normal distance from the bed surface to the position where the velocity components are measured, and v_t is the eddy viscosity taken as 1.3×10^{-5} m^2/s.

The specific Reynolds shear stresses, τ_{13}, at 14 locations (f1 to f7 and b1 to b7, marked in Figure 4.2) upstream and downstream of the pier in the plane through the channel centerline are plotted as vertical profiles in Figures 5.9a,b. Upstream of the pier, τ_{13} remains approximately linear outside the scour hole (the solid black curve at location f7, showing little vertical variations); all the other profiles show large variations near the bed, the f5 profile being the most dramatic (Figure 5.9a). Downstream of the pier, τ_{13} has relatively high values near the surface and near the bed; overall the τ_{13} values are lower than those upstream of the pier.

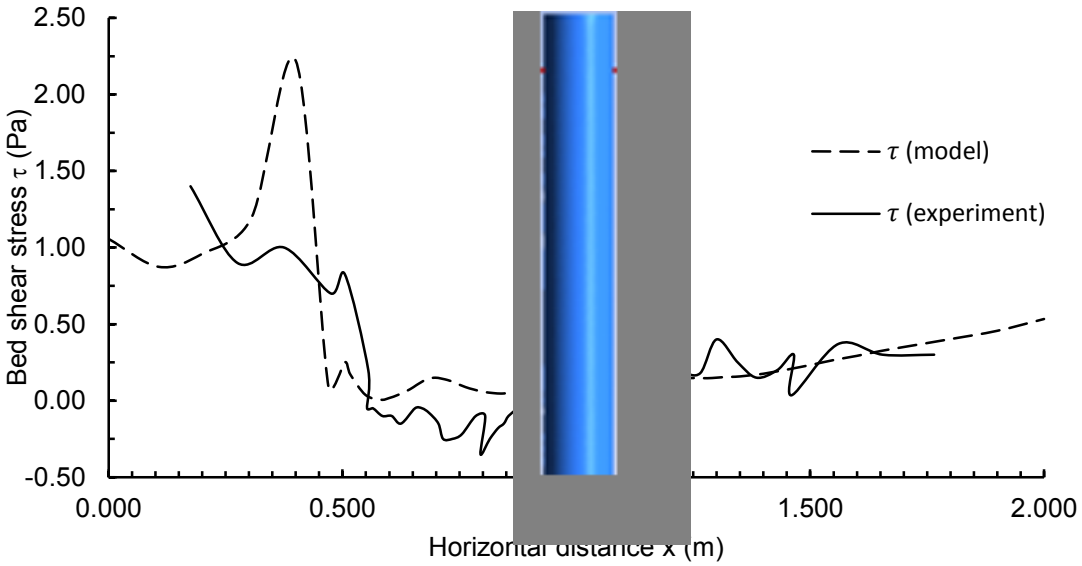

Figure 5.8 A comparison of the bed shear stress between model prediction and experimental data.

The vertical distributions of the turbulence kinetic energy, k [equation (3.15)], normalised by the shear velocity, $u_* \equiv (\tau_b/\rho)^{0.5}$, are plotted in Figures 5.10a,b for two planes 0.2 m or 1.33D upstream and downstream of the pier. The value for u_* was reported as 2.65 cm/s in Graf and Istiarto (2002). The normalised k/u_* values are small from the free surface down to a depth of 2D, both upstream and downstream of the pier. The k/u_* values increase by six-fold near the bed upstream of the pier. Downstream of the pier, relatively speaking, k/u_* has higher values near the surface, possibly in association with flow separation.

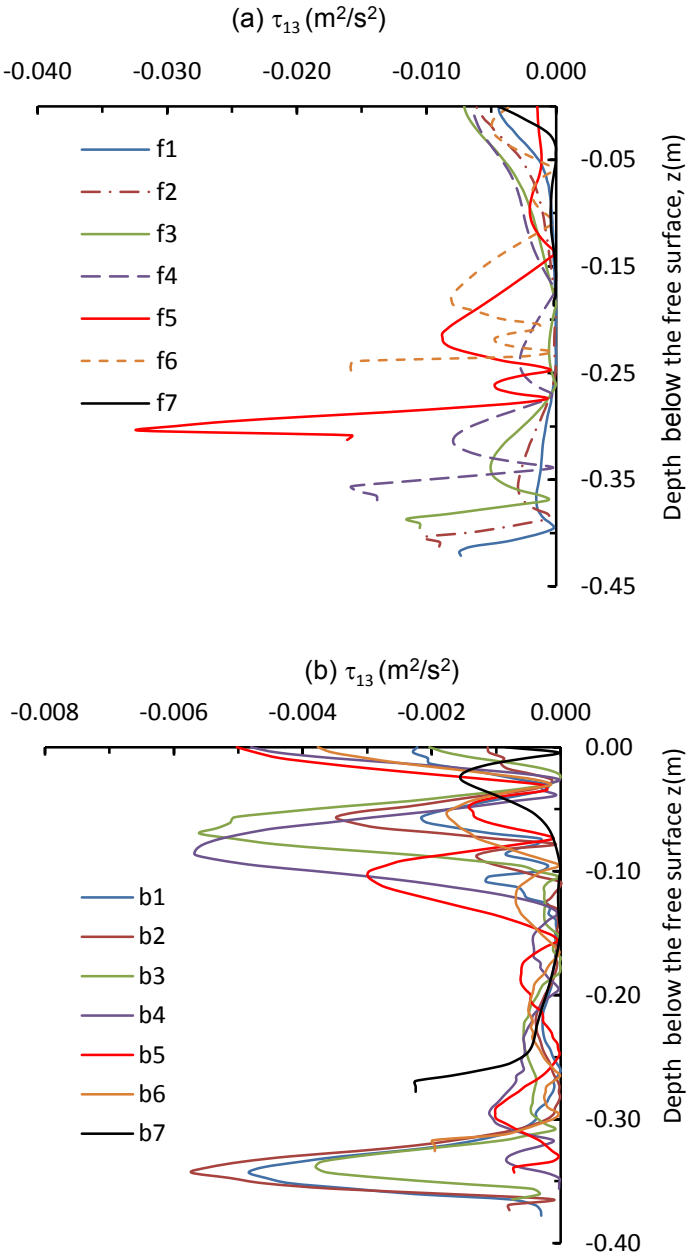

Figure 5.9 Vertical profiles of the specific Reynolds shear stress at 14 selected locations marked in Figure 4.2.

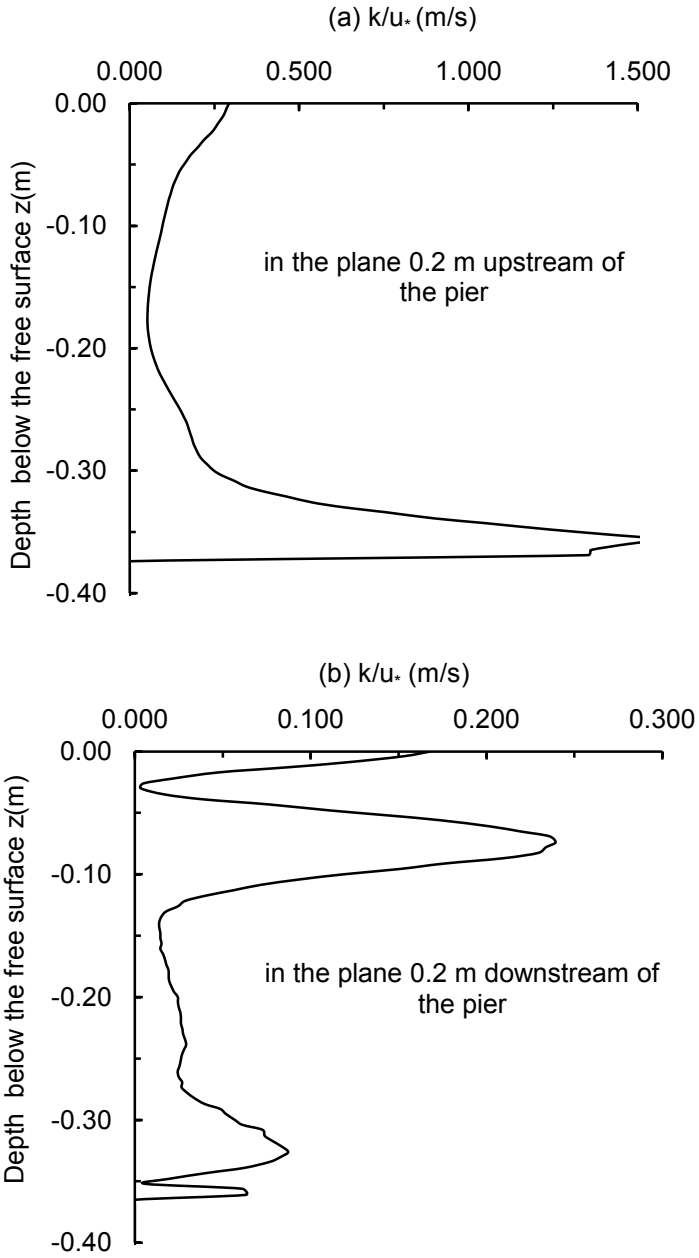

Figure 5.10 Distributions of normalized turbulence kinetic energy in two representative planes.

5.2 The SPH model

5.2.1 Sensitivity test simulations and approach flow

Test simulations were carried out for three purposes: (a) to ensure that the inflow to the main channel (below the gate, Figure 4.3) or the approach flow is consistent with that in Graf and Istiarto's (2002) experiments, i.e. the inflow is steady for a certain period of time, and has a depth-averaged velocity of 0.45 cm/s and a depth of 0.18 m; (b) to confirm that the reduction in width of the main channel to increase computational efficiency (discussed in Section 4.2) does not have significant artificial effects on the flow field in the scour hole; (c) to ensure that the installation of an artificial lid on the top of the main channel does not result in unrealistic velocity profiles between the water surface (in the experiments) and the channel-bed.

Consistent inflow has successfully been produced by systematically adjusting the dimensions of the upstream reservoir (Figure 4.3), fluid volume, distance between smoothed fluid particles and some of the parameters listed in Table 4.2. These quantities are all purely numerical, as discussed in Sections 4.2 and 4.3. As illustrated by the time series of flow velocities in Figure 5.11, the inflow becomes quasi-steady after 100 time steps and remains steady over a sufficiently long time period (say between time steps 100 and 200). At the middle depth (0.09 m above the channel-bed in a 0.18 m water column), the inflow has a velocity of 0.451 m/s, which is very close to the approach flow velocity in the experiments.

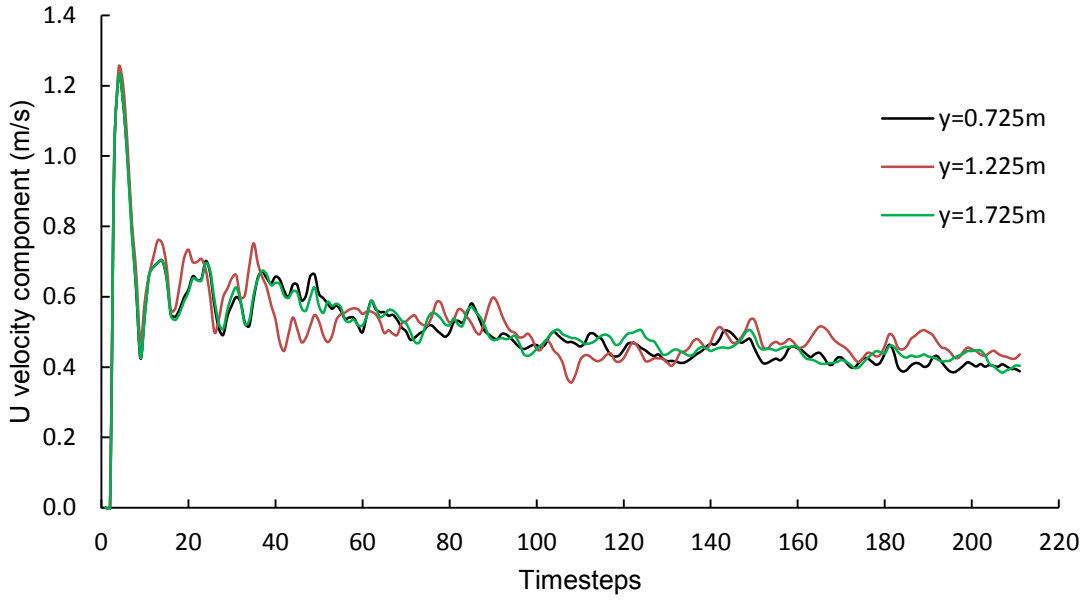

Figure 5.11 Time series of longitudinal flow velocities at three different locations below the gate of the upstream reservoir (Figure 4.3). The z coordiates of these locations are 0.09 m (or 0.09 m above the channel-bed).

An examination of the model results (not shown) for a number of test simulations, where the main channel had different widths, shows no significant effects on the velocity field upstream and downstream of the scour hole in the main channel and within the scour hole around the pier. Thus, 5D was taken as the width on both sides of the pier.

Through test simulations, it has been confirmed that predicted velocity profiles (Figure 5.12) do not have unrealistic shape in the presence of an artificial lid on the top of the main channel. From the peak velocity location (Figure 4.5), which represents the free surface in the experiments, to the channel-bed, the flow velocity decreases with increasing distance below the water surface. The profiles show a velocity of 0.451 m/s at the middle depth (z = 0.09 m), with the depth-averaged

velocity matching well the experimental condition in Graf and Istiarto (2002). Therefore, it was concluded that the SPH model has been properly setup for the application.

Note that similar to FEM simulations, all the SPH simulations begin from a state of rest. Initially, the model channels, including the main channel and downstream channel extension, are filled with water. The use of this initial condition, along with the use of a lid, helps force water entering the scour hole and flowing around the pier (Figure 4.3), which is difficult to achieve in dam-break type of simulations. In the following, SPH results were presented at time step 198 or 5.94 s of model time.

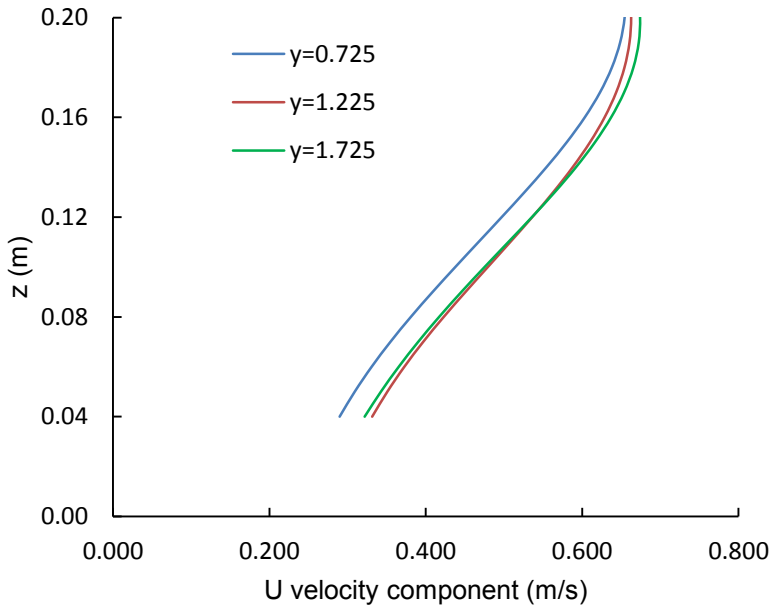

Figure 5.12 Vertical distributions of longitudinal velocity at three locations below the gate (Figure 4.3) at the time step 198 or at 5.94 s of model time. The data gap in the bottom 4 cm distance is due to SPH limitation with respect to solid boundaries.

5.2.2 Velocity vector field in the horizontal plane

Velocity vectors in the horizontal plane at the mid-depth (or z = 0.09 m) are shown in Figure 5.13. It is possible to make a number of observatons: (a) Water flow passing though the gate (at x = 0 m) reamains parallel in a straightline to the channel-bed (not covered in Figure 5.13) except in regions near the two sidewalls (at y = 0.40 and 2.05 m, respectively), where the flow direction shows some variation from the straight path; (b) near the upstream nose of the pier, flow velocity changes in both magnitude and direction; (c) some circulations due to wake vortices are visible just downstream of the pier; (d) further downstream, velocity vectors regain uniformity (the figure does not cover that far downstream). The velocity vectors upstream of the pier show similar flow patterns as those in Figure 5.1. The velocity vectors downstream show less details about wake vortices compared to Figure 5.1.

5.2.3 Velocity vector field in the vertical plane

In Figure 5.14, a plot of velocity vectors in the vertical plane along the centreline of the main channel (Figure 4.3). As the inflow results from a sudden lifting of the gate (somewhat like a dam-break), velocity vectors just downstream of the gate are not perpendicular to the gate (not covered in Figure 5.14). Water flows though the main channel and enters the scour hole, where velocity vectors have a downward component. As the flow approaches the pier, a down flow occurs just upstream of the pier. Downstream of the pier, the flow weakens with small velocities at different directions. Further downstream in the scour hole, the velocity vectors are more or less parallel to the local rising bed profile and accelerate.

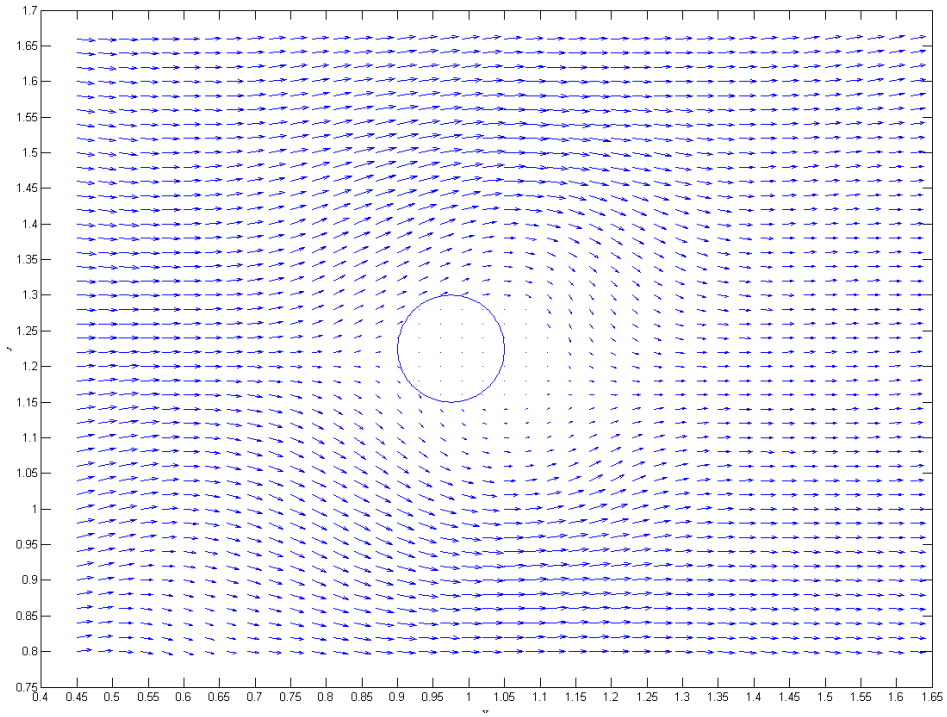

Figure 5.13 A horizontal plane showing velocity vectors at a depth of 0.09 m below the free surface.

5.2.4 Vertical profile of longitudinal velocity

Vertical profiles of the longitudinal velocity obtained from SPH simulations at seven locations (f1 to f7, Figure 4.2) upstream of the pier are plotted in Figure 5.15a. The velocity decreases as the flow approaches the pier. The decrease is because of the pier being in the flow path and results in downward motions. The profiles at locations f5, f6 and f7 show more profound vertical structures. Inside the scour hole, all the profiles (Figure 5.15b) show negative values for the vertical component of velocity W or downward velocities. The downward velocity at location f5 is the strongest ($\approx 0.46u_o$ as the maximum). The downward velocities intensify with depth, reach a maximum at the middle depth and then weaken towards the channel-bed.

The velocity profile outside the scour hole at location f7 shows weak upward velocities.

Downstream of the pier, longitudinal velocities (Figure 5.16a) are positive. In general the velocities increase with distance toward downstream, which is particularly the case near the free surface. As the flow accelerates over the rising channel-bed, velocity near the bed increases probably. With respect to the vertical component of velocity W (Figure 5.16b), it is upward at all locations except at location b1 and b2 or in very close distance from the pier.

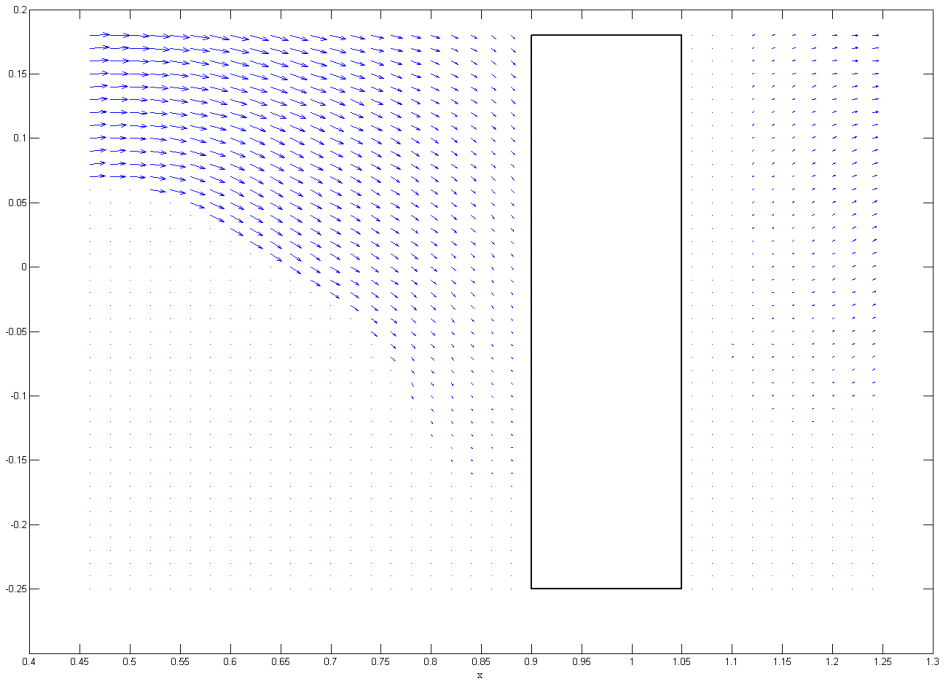

Figure 5.14 Velocity vectors in the vertical plane through the channel centreline.

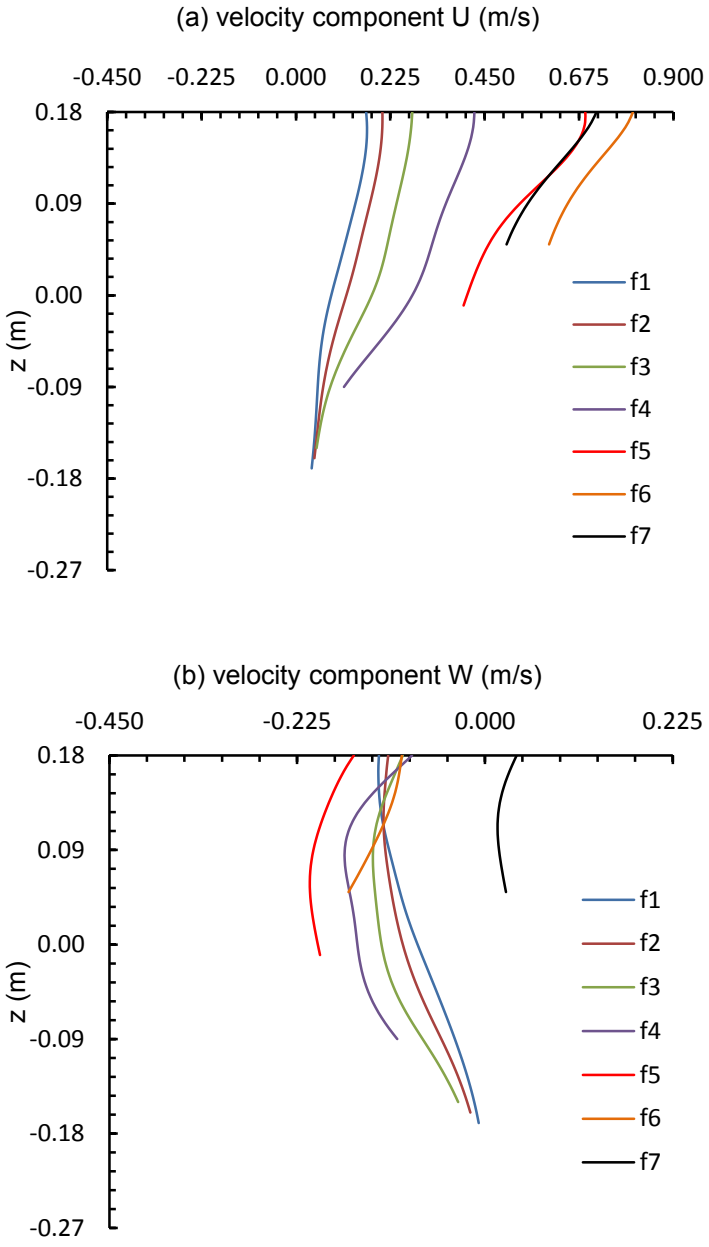

Figure 5.15 Vertical profiles of the x-component (panel a) and z-component (panel b) of velocity at seven selected locations (labeled as f1 to f7 in Figure 4.2) upstream of the pier. In the approach channel, the channel-bed is located at z = 0 m.

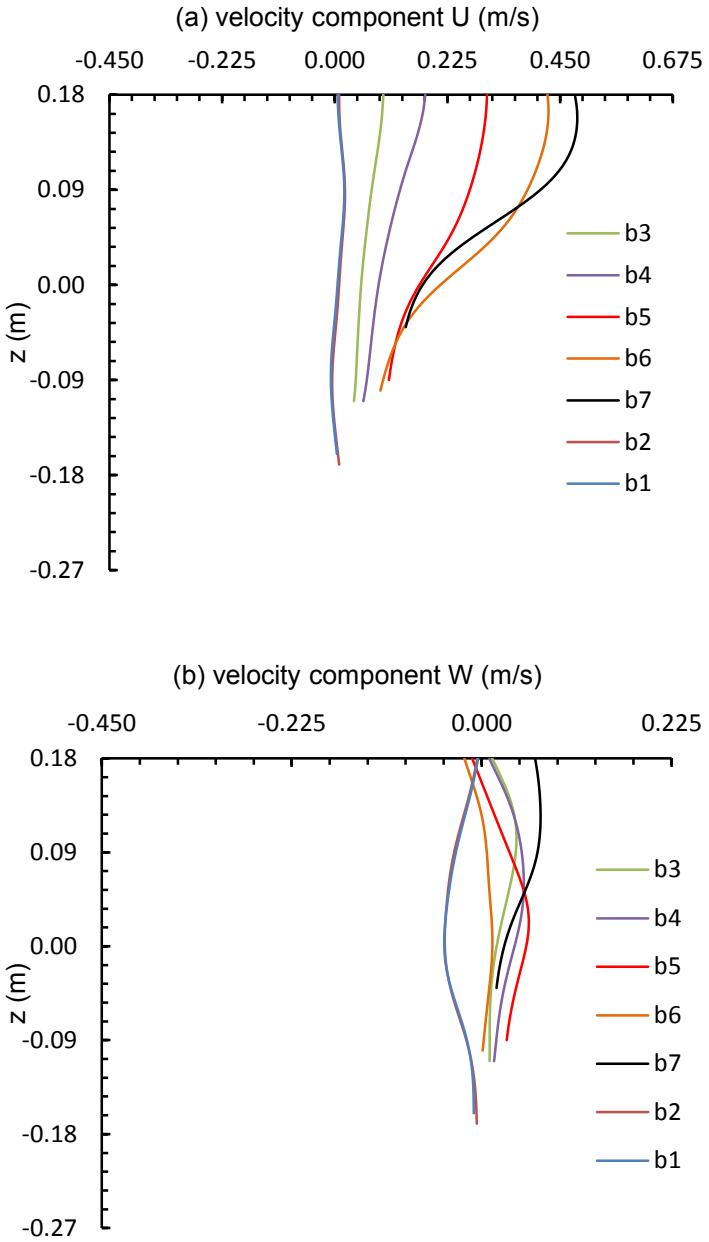

Figure 5.16 Vertical profiles of the x-component (panel a) and z-component (panel b) of velocity at 7 selected locations (labeled as b1 to b7 in Figure 4.2) downstream of the pier. In the approach channel, the channel-bed is located at z = 0 m.

5.2.5 Comparison of vertical profiles between SPH, FEM and experiments

In Figure 5.17, vertical profiles of the longitudinal velocity from both SPH and FEM simulations at the seven locations (f1 to f7, Figure 4.2) upstream of the pier are

compared with laboratory measurements (Graf and Istiarto, 2002). The comparison appears to be reasonable, especially at locations f1, f2, f3 and f4 (Figures 5.17a-d) near the pier (Figure 4.2). At location f7 (Figure 5.17g) outside the scour hole, both the model predicted velocities are too large, compared to measurements. At the location f6 near the upstream edge of the scour hole, predicted velocities from SPH are larger than FEM simulated velocities and experimental measurements. The measurements do not cover the upper water column at locations f1, f2 and f3.

Comparisons of simulated and measured vertical velocities are shown in Figure 5.18. The FEM and SPH models predict downward flow at all the locations except f7, where SPH results have positive vertical velocities. This prediction is supported by measurements, although there are discrepancies in magnitude.

5.3 Comparison between FEM and SPH

FEM, a mesh-based hydrodynamics model, and SPH, a mesh-free hydrodynamics model, have been applied to the bridge hydraulics problem of free-surface flow around a circular pier in a fixed scour hole. In FEM, the built-in DesignModeler within the ANSYS workbench was really a user-friendly tool to build the geometry with provisions of making lots of modification. This makes it easier to create the complex geometry precisely. On the other hand, in SPH, the geometry was developed with other available drawing or geometry development tools.

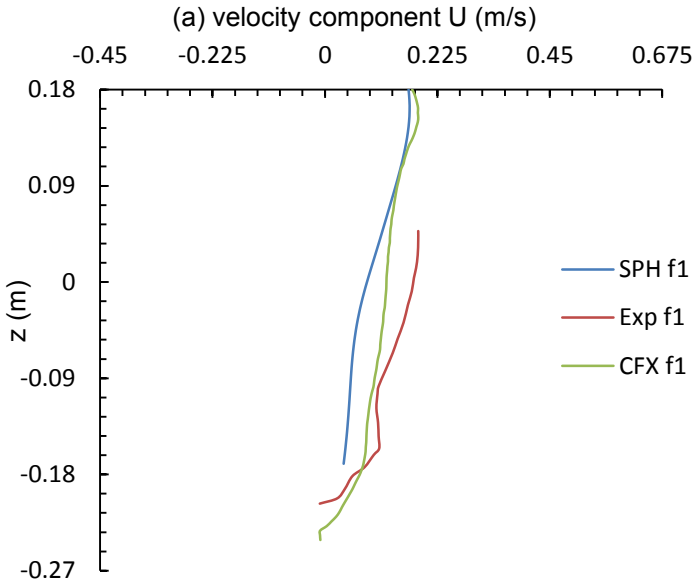
(a) velocity component U (m/s)
-0.45
-0.225
0
0.225
0.45
0.675
0.18
0.09
0
-0.09
-0.18
-0.27
z (m)
SPH f1
Exp f1
CFX f1

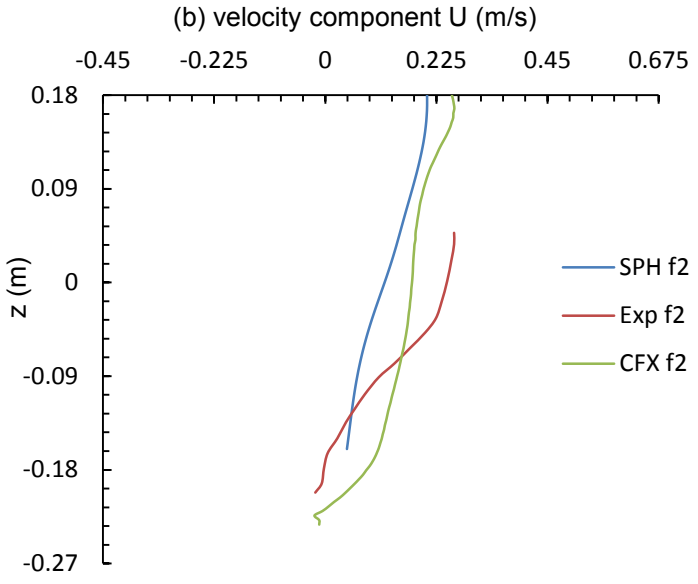
(b) velocity component U (m/s)
-0.45
-0.225
0
0.225
0.45
0.675
0.18
0.09
0
-0.09
-0.18
-0.27
z (m)
SPH f2
Exp f2
CFX f2

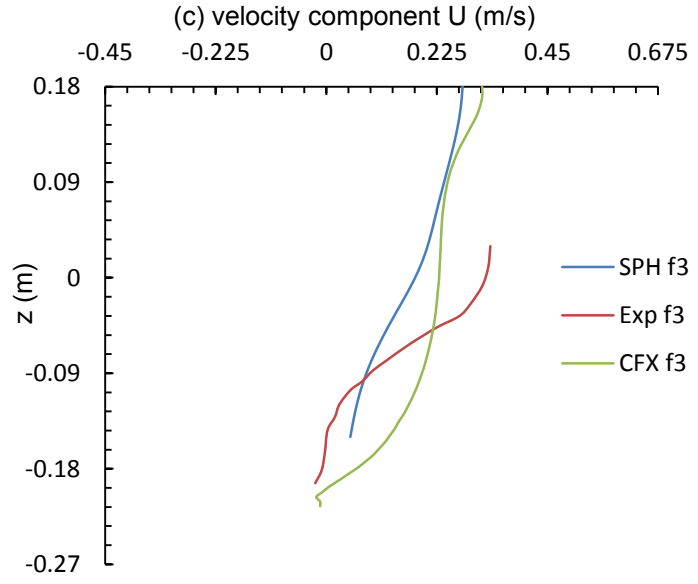
(c) velocity component U (m/s)
-0.45
-0.225
0
0.225
0.45
0.675
0.18
0.09
0
-0.09
-0.18
-0.27
z (m)
SPH f3
Exp f3
CFX f3

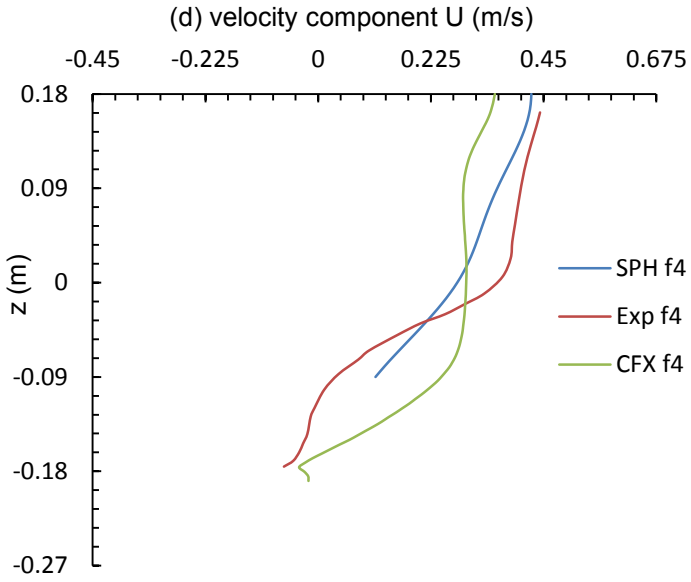
(d) velocity component U (m/s)
-0.45
-0.225
0
0.225
0.45
0.675
0.18
0.09
0
-0.09
-0.18
-0.27
z (m)
SPH f4
Exp f4
CFX f4

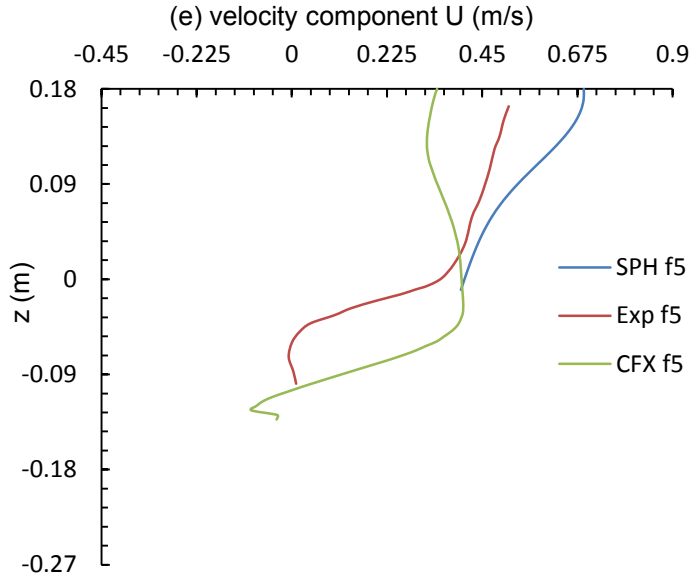
(e) velocity component U (m/s)
-0.45
-0.225
0
0.225
0.45
0.675
0.9
0.18
0.09
0
-0.09
-0.18
-0.27
z (m)
SPH f5
Exp f5
CFX f5

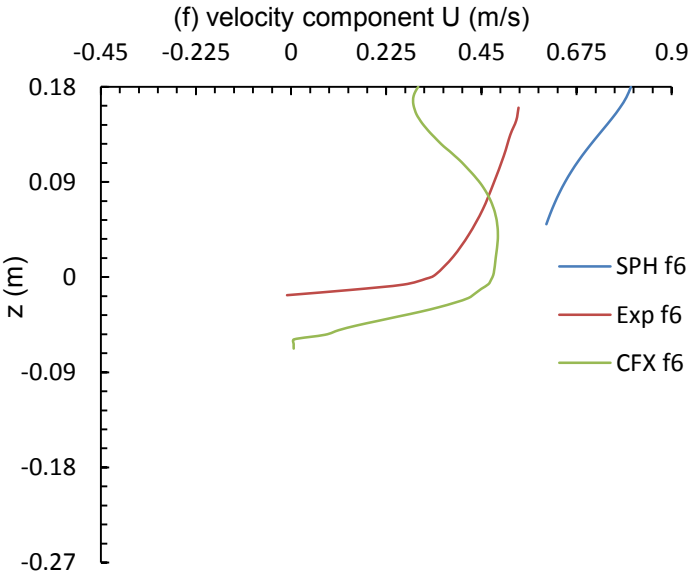
(f) velocity component U (m/s)
-0.45
-0.225
0
0.225
0.45
0.675
0.9
0.18
0.09
0
-0.09
-0.18
-0.27
z (m)
SPH f6
Exp f6
CFX f6

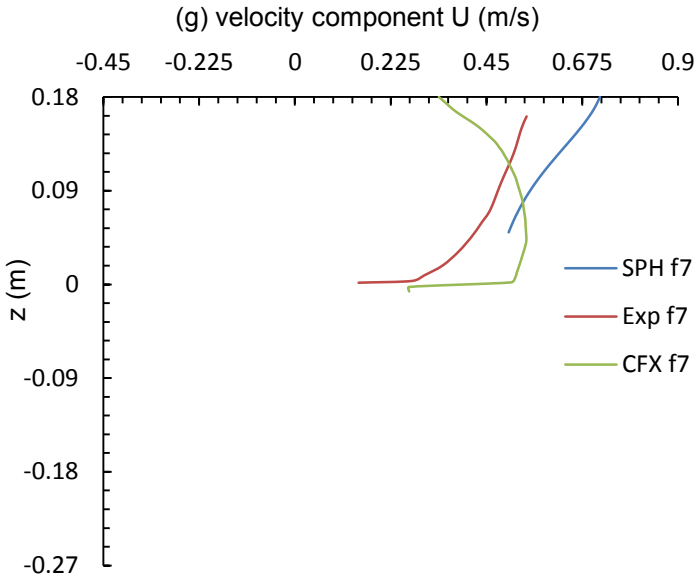

Figure 5.17 Comparison of the longitudinal velocity among FEM, SPH and experimental measurements (Graf and Istiarto, 2002) at selected locations upstream of the pier.

For simulations using FEM, a mesh size should be defined with a proper selection of mesh type and other control features. This brings the inaccuracy in the sense that with a coarser mesh, near-boundary complex flow features are impossible to predict. In other words, one losses the near-boundary flow features when using a coarser mesh. In principle, one may use a finer mesh size to adequately resolve the near-boundary flow, but the required overall computational memory increases significantly, which makes it computationally inefficient. In this case, application of inflation layers in the boundary mesh resolves some part of the near-boundary flow. On the contrary, SPH does not need any mesh as it is a mesh-free method. The flow field in SPH is associated with the trajectory of each particle. Therefore there is no numerical diffusion, which is advantageous over mesh-based methods.

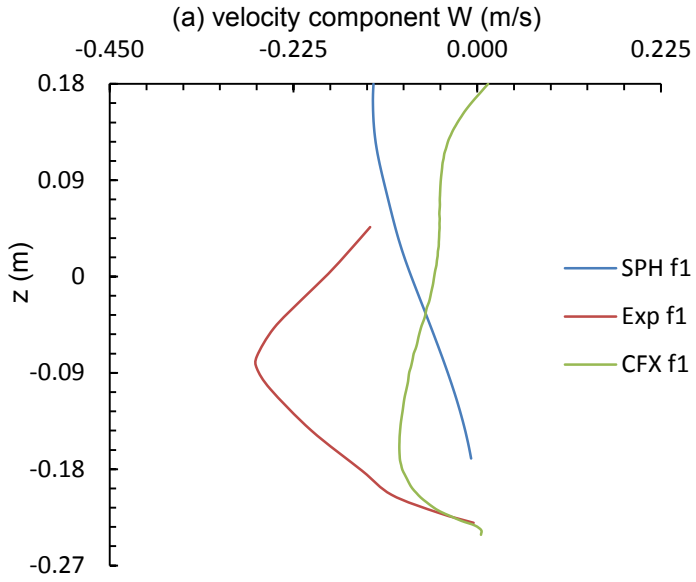
(a) velocity component W (m/s)
-0.450
-0.225
0.000
0.225
0.18
0.09
0
-0.09
-0.18
-0.27
z (m)
SPH f1
Exp f1
CFX f1

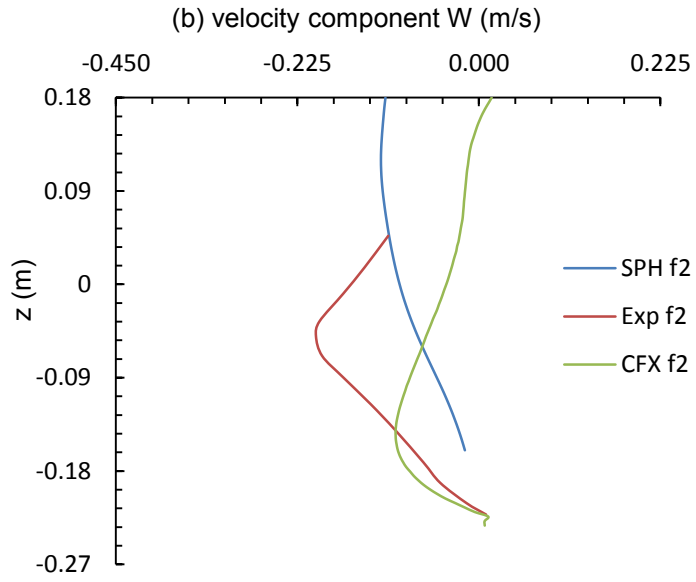
(b) velocity component W (m/s)
-0.450
-0.225
0.000
0.225
0.18
0.09
0
-0.09
-0.18
-0.27
z (m)
SPH f2
Exp f2
CFX f2

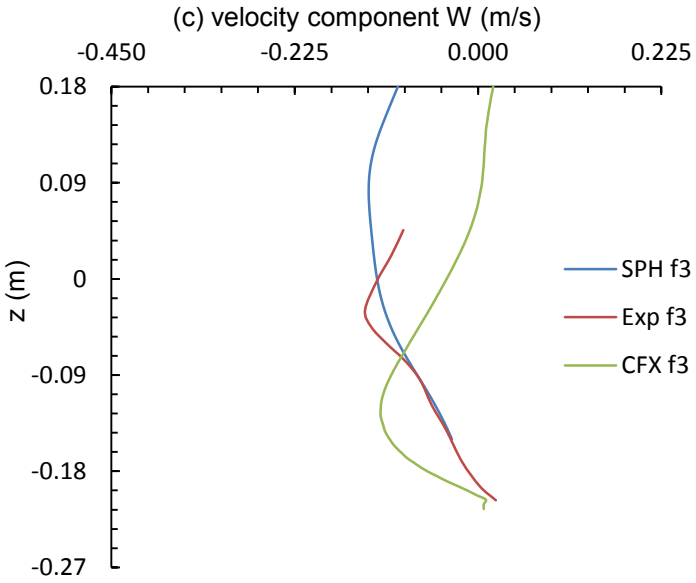
(c) velocity component W (m/s)
-0.450
-0.225
0.000
0.225
0.18
0.09
0
-0.09
-0.18
-0.27
z (m)
SPH f3
Exp f3
CFX f3

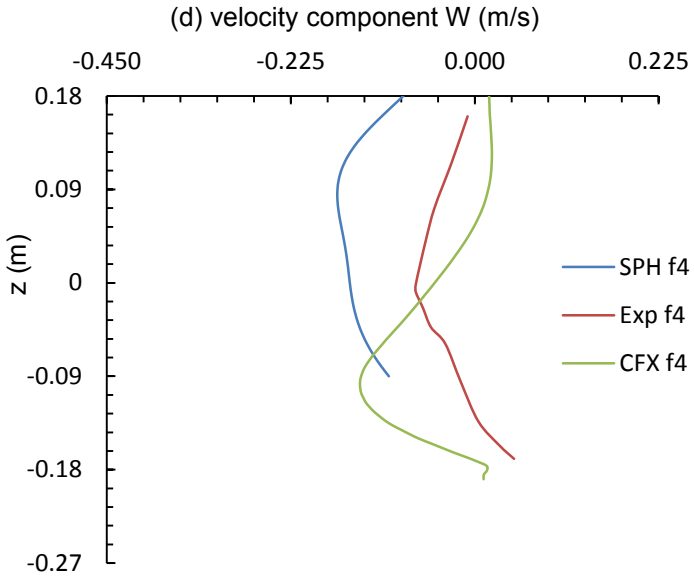
(d) velocity component W (m/s)
-0.450
-0.225
0.000
0.225
0.18
0.09
0
-0.09
-0.18
-0.27
z (m)
SPH f4
Exp f4
CFX f4

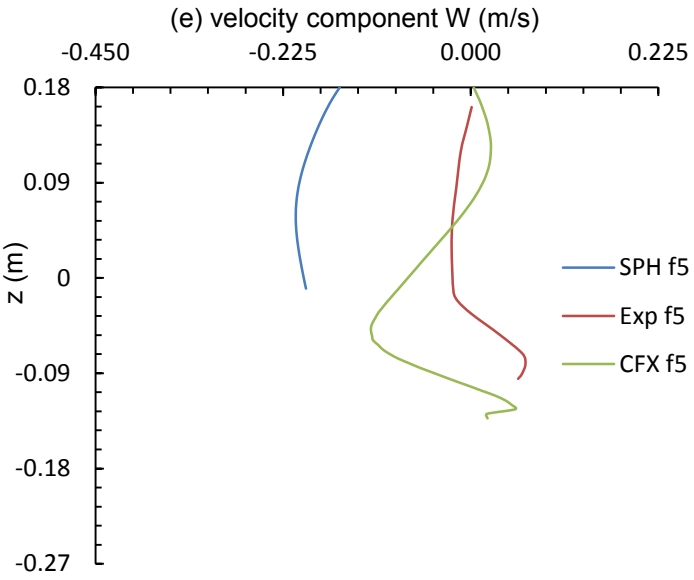
(e) velocity component W (m/s)
-0.450
-0.225
0.000
0.225
0.18
0.09
0
-0.09
-0.18
-0.27
z (m)
SPH f5
Exp f5
CFX f5

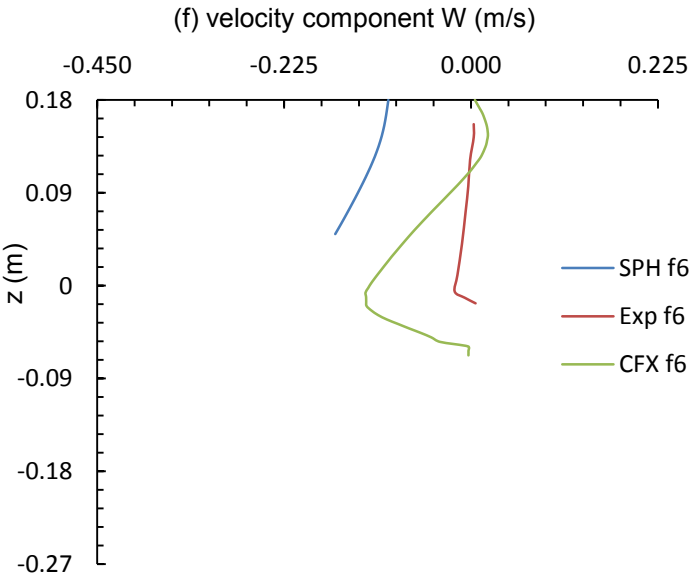
(f) velocity component W (m/s)
-0.450
-0.225
0.000
0.225
0.18
0.09
0
-0.09
-0.18
-0.27
z (m)
SPH f6
Exp f6
CFX f6

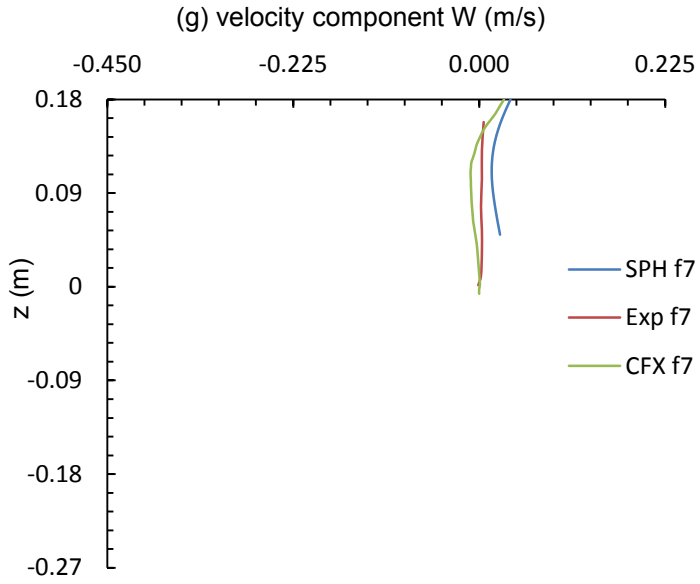

Figure 5.18 Comparison of the vertical velocity among FEM, SPH and experimental measurements (Graf and Istiarto, 2002) at selected locations upstream of the pier.

In application of SPH to the bridge hydraulics problem using the existing SPH code, it was not possible to specify uniform inflow at the entrance or inlet of the main channel, which is rather implementation of SPH in SPHysics and its derivatives. In FEM, there are different choices of inflow condition specification. Based on the results presented in Sections 5.1 and 5.2, FEM appears to be more robust in determining the flow within the scour hole and around the pier. The velocity vectors and vertical velocity profiles based on FEM simulation output have shown vortices and eddy motions of different length scale commendably. Also, FEM has been computationally more efficient than SPH; FEM needed less computational time to produce results for the given conditions in this modelling research. SPH needs modification for application to the bridge hydraulics problem.

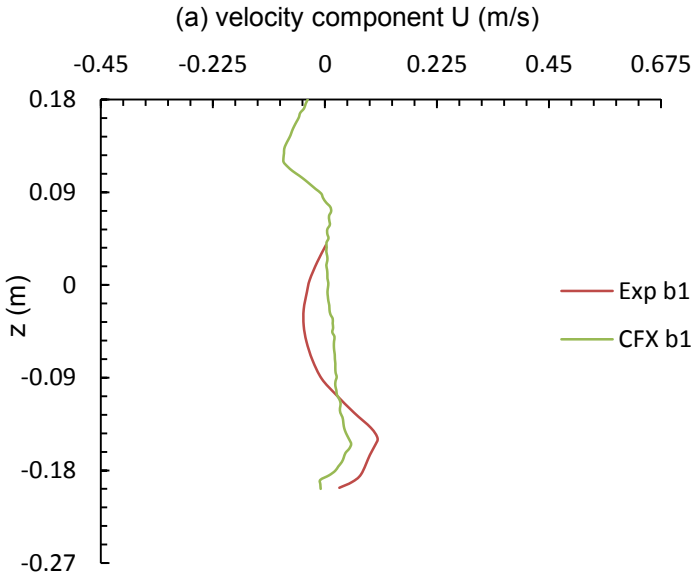
(a) velocity component U (m/s)
-0.45
-0.225
0
0.225
0.45
0.675
0.18
0.09
0
-0.09
-0.18
-0.27
z (m)
Exp b1
CFX b1

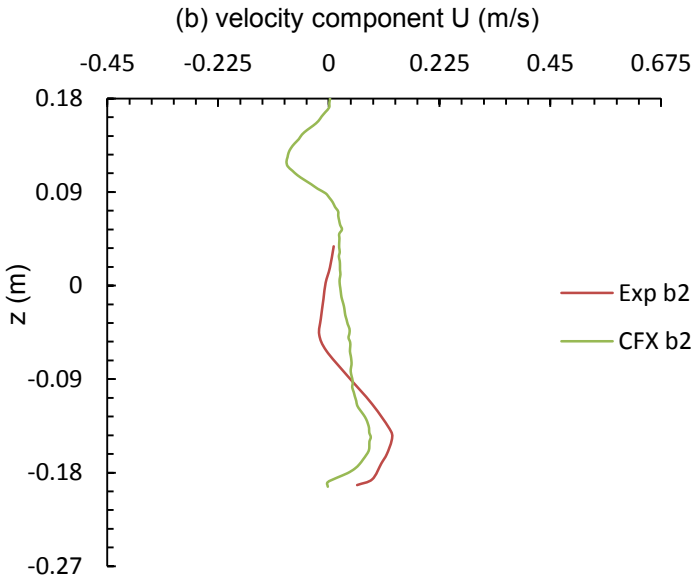
(b) velocity component U (m/s)
-0.45
-0.225
0
0.225
0.45
0.675
0.18
0.09
0
-0.09
-0.18
-0.27
z (m)
Exp b2
CFX b2

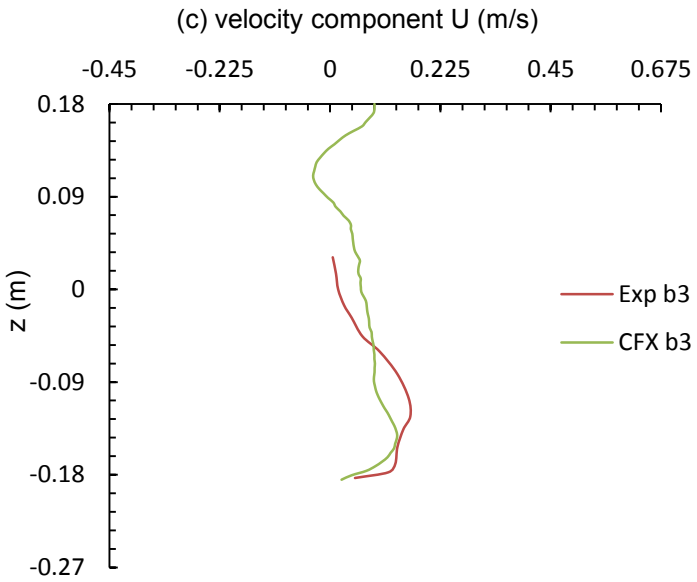
(c) velocity component U (m/s)
-0.45
-0.225
0
0.225
0.45
0.675
0.18
0.09
0
-0.09
-0.18
-0.27
z (m)
Exp b3
CFX b3

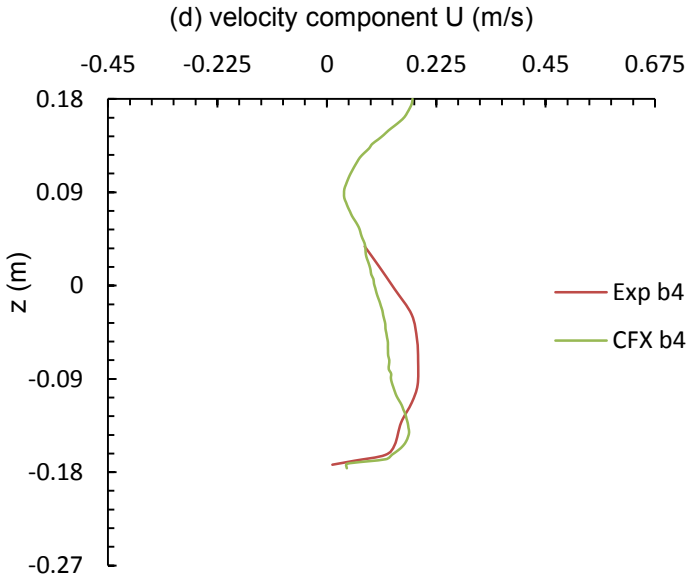
(d) velocity component U (m/s)
-0.45
-0.225
0
0.225
0.45
0.675
0.18
0.09
0
-0.09
-0.18
-0.27
z (m)
Exp b4
CFX b4

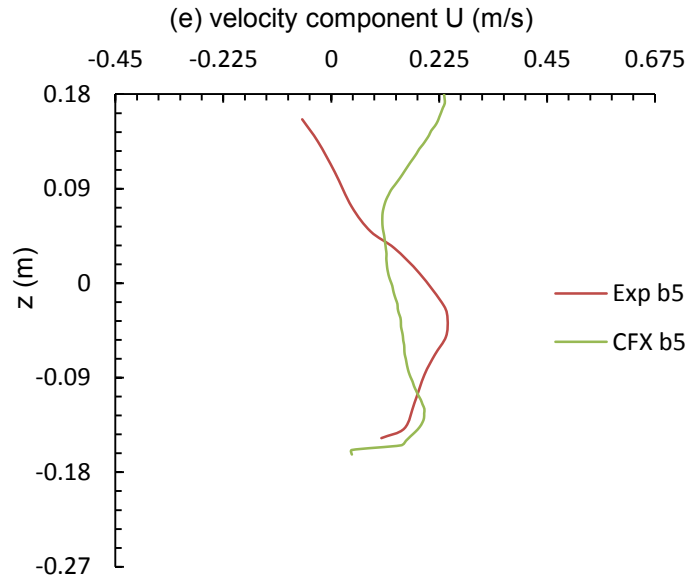
(e) velocity component U (m/s)
-0.45
-0.225
0
0.225
0.45
0.675
0.18
0.09
0
-0.09
-0.18
-0.27
z (m)
Exp b5
CFX b5

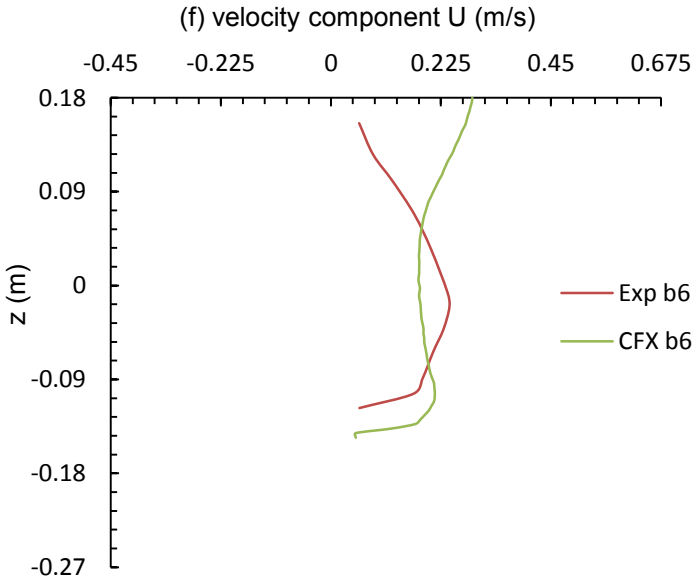
(f) velocity component U (m/s)
-0.45
-0.225
0
0.225
0.45
0.675
0.18
0.09
0
-0.09
-0.18
-0.27
z (m)
Exp b6
CFX b6

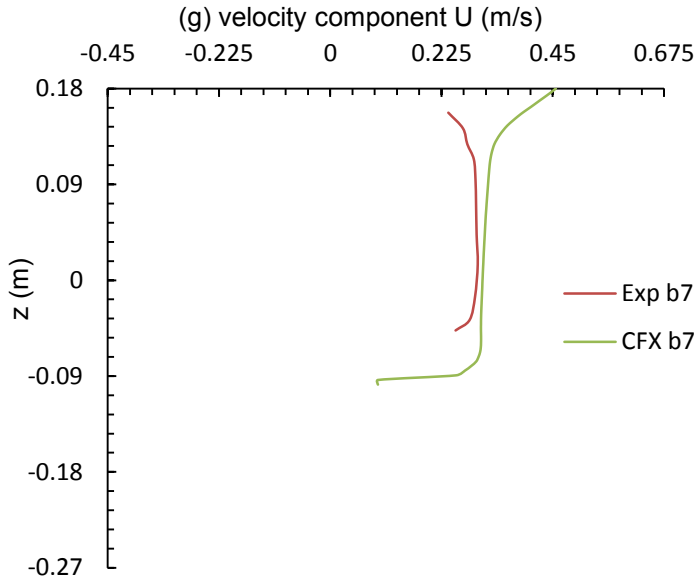

Figure 5.19 Comparison of the longitudinal velocity among FEM and experimental measurements (Graf and Istiarto, 2002) at selected locations downstream of the pier.

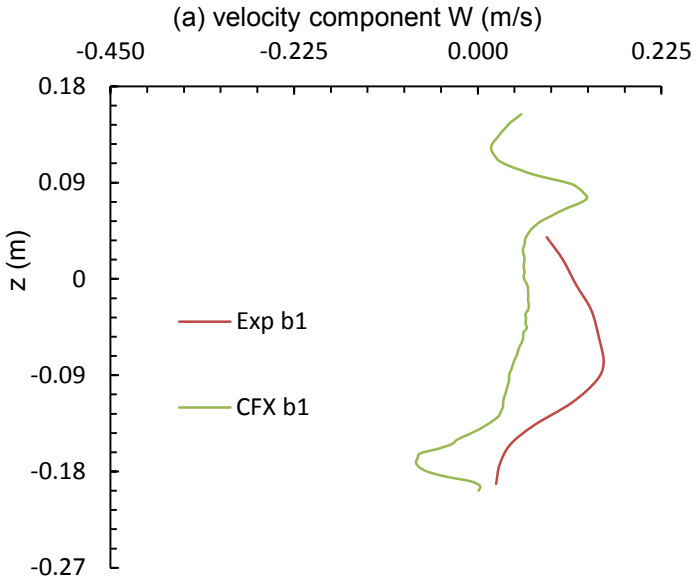
(a) velocity component W (m/s)
-0.450
-0.225
0.000
0.225
0.18
0.09
0
-0.09
-0.18
-0.27
z (m)
Exp b1
CFX b1

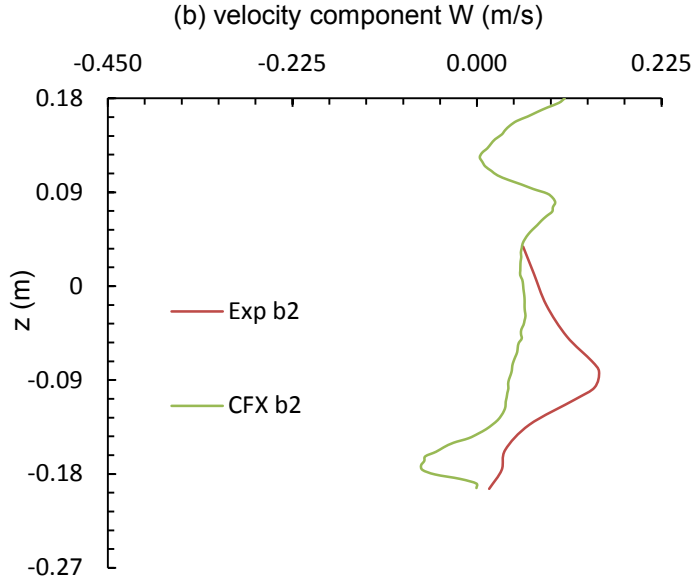
(b) velocity component W (m/s)
-0.450
-0.225
0.000
0.225
0.18
0.09
0
-0.09
-0.18
-0.27
z (m)
Exp b2
CFX b2

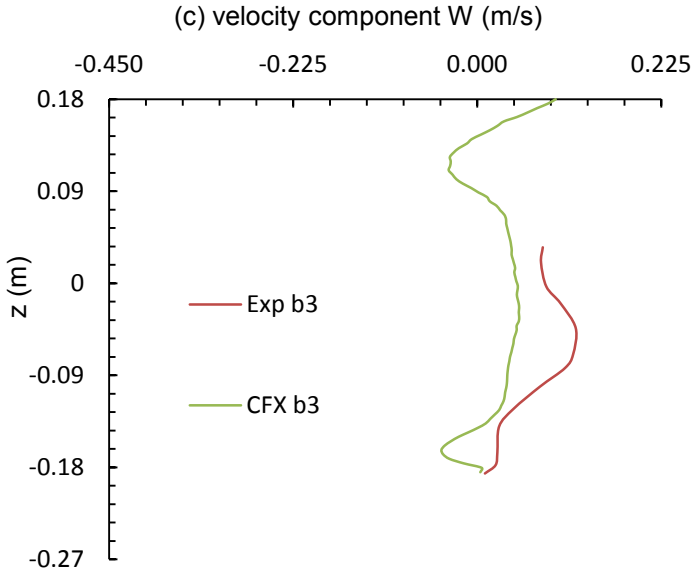
(c) velocity component W (m/s)
-0.450
-0.225
0.000
0.225
0.18
0.09
0
-0.09
-0.18
-0.27
z (m)
Exp b3
CFX b3

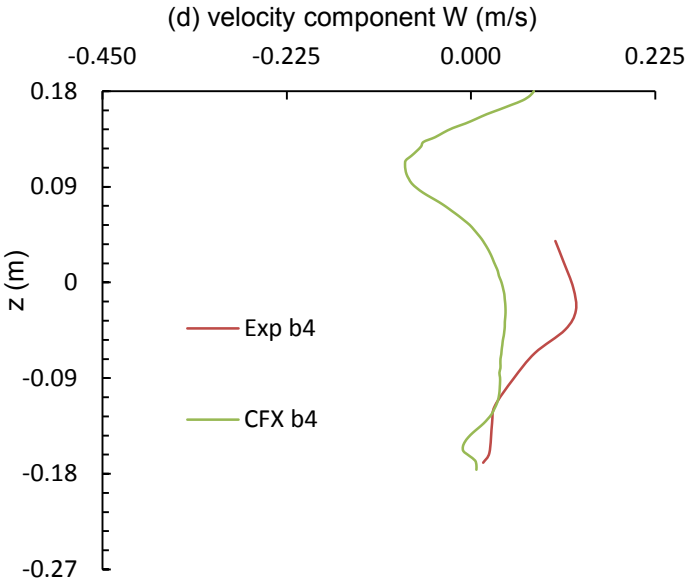
(d) velocity component W (m/s)
-0.450
-0.225
0.000
0.225
0.18
0.09
0
-0.09
-0.18
-0.27
z (m)
Exp b4
CFX b4

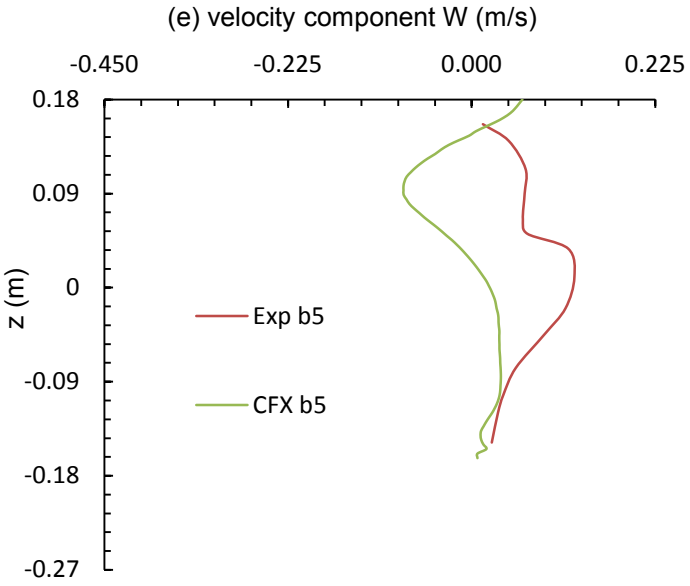
(e) velocity component W (m/s)
-0.450
-0.225
0.000
0.225
0.18
0.09
0
-0.09
-0.18
-0.27
z (m)
Exp b5
CFX b5

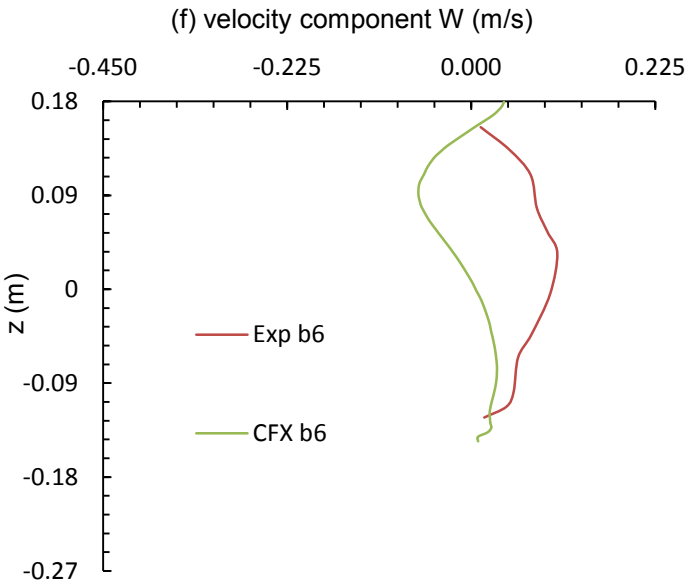
(f) velocity component W (m/s)
-0.450
-0.225
0.000
0.225
0.18
0.09
0
-0.09
-0.18
-0.27
z (m)
Exp b6
CFX b6

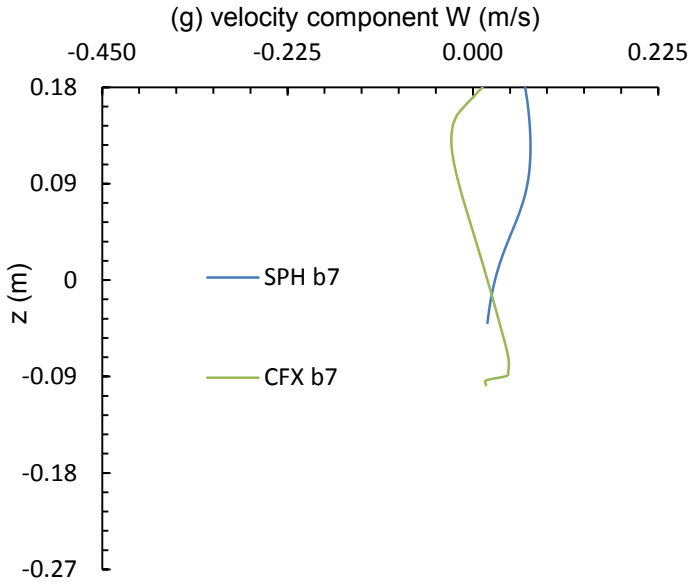

Figure 5.20 Comparison of the vertical velocity among FEM and experimental measurements (Graf and Istiarto, 2002) at selected locations downstream of the pier.

Chapter Six Conclusion

6.1 Concluding remarks

River flow has caused significant bridge pier scour, and resulted in many bridge failures. This research focuses on the problem of scour-inducing turbulent flow passing around a circular pier in a fixed scour hole. For given hydraulic conditions and geometric parameters, numerical prediction of the flow field has been obtained with FEM, a mesh-based hydrodynamics model. SPH, a mesh-free hydrodynamics model has also been applied for the same hydraulic conditions and geometric parameters as a complementary. The prediction from FEM model is in reasonable quantitative comparison with available laboratory measurements (Graf and Istiarto, 2002). An analysis of the results from the two numerical models leads to the following conclusion:

(1) FEM prediction is shown to capture some detailed features of the flow field in a realistic manner, including strong vortices at the foot of the pier on the upstream side, and eddy motions in the wake region. These details are absent from the SPH results. Two possible reasons are: (a) the use of an artificial lid on the top of the model channel in order to force particles to reach deeper in the scour hole; (b) the use of a relatively large distance between particles so as to maintain manageable computational costs. Eddy motions of length scale shorter than the distance cannot be resolved.

(2) Prediction of bed shear stress as direct output from FEM agrees well with the measurements. Some discrepancies exist for locations just before water

enters the scour hole. FEM prediction of the near-bed turbulence kinetic energy is realistic. These predictions are useful for the calibration of sediment transport models.

(3) On the basis of FEM simulations, downstream of the pier, flow separation and complex vortex stretching take place but appear to be confined to the upper water column. This finding is new. The confinement may be explained as follows: Downstream of the pier, the near-bed flow accelerates over the rising bed, which would create a favorable pressure gradient and therefore tends to suppress flow separation. Clockwise and counter-clockwise wake vortices in the horizontal are visible over a large distance (many times the pier diameter) from the pier.

(4) On the basis of FEM simulations, upstream of the pier, the turbulent kinetic energy increases by six-fold near the bed from the value near the free surface. Downstream of the pier, the turbulent kinetic energy has higher values near the free surface than near the bed, possibly due to flow separation in the upper water column.

(5) Both models predict a downflow near the upstream nose of the pier. This prediction is supported by the measurements. Comparisons between predicted and measured velocity profiles at a series of locations upstream of the pier are acceptable. The downflow has important implications for the safe design of pier foundations.

(6) This research is successful in generating desired approach flow in SPH application to the bridge hydraulics problem, by adjusting the dimensions of the upstream reservoir, distance between particles and time step. Together

with the idea of symmetry, the approach flow maintains a steady state, attains a realistic velocity profile and flow depth, and gives a required total discharge.

6.2 Suggestion for future research

This study has used uniform approach flow in FEM simulations. Future studies should consider the influence of distributed flow velocities at the inlet and remove the assumption that the energy coefficient is unity. In the setup of SPH simulations, this study has treated the approach flow as a dam break scenario. Future SPH modelling studies should improve the specification of approach flow for application to bridge hydraulics problems. Also SPH modelling with implementation of turbulence closure schemes is expected to give more accurate measure of turbulence and flow field within the scour hole around bridge pier. More laboratory and field measurements of flow velocity around bridge piers will be useful for validation of both mesh-based and mesh-free models.

References

Ahmed, F. and Rajaratnam, N. (1998) “Flow around bridge piers.” *Journal of Hydraulic Engineering,* ASCE, 24:288-300.

Ali, K. H. M., Karim, O. A. and Connor, B. A. (1997) “Flow patterns around bridge piers and offshore structures.” *Proceedings of Water Resources Engineering Conference*, ASCE, San Francisco, USA, 208–213.

ANSYS, Inc. (2011) *ANSYS CFX-Solver Theory Guide,* Release 14.0, Southpointe, Canonsburg, PA, USA.

Beheshti, A.A. and Ataie-Ashtiani, B. (2010) “Experimental study of three-dimensional flow field around a complex bridge pier.” *Journal of Engineering Mechanics,* ASCE, 136:143-154.

Breusers, H. N. C., Nicollet, G. and Shen, H. W. (1977) “Local scour around cylindrical piers.” *Journal of Hydraulic Research*, 15:211-252.

Chang, T., Kao, H., Chang, K. and Hsu, M. (2011) “Numerical simulation of shallow-water dam break flows in open channels using smoothed particle hydrodynamics.” *Journal of Hydrology*, Elsevier, 408: 78-90.

Crespo, A.J.C., Gomez-Gesteira, M. and Dalrymple, R.A. (2007) “3D SPH Simulation of large waves mitigation with a dike.” *Journal of Hydraulic Research*, IAHR, 45(5):631-642.

Crespo, A.J.C., Gomez-Gesteira, M. and Dalrymple, R.A. (2008) “Modeling Dam Break Behavior over a Wet Bed by a SPH Technique.” *Journal of Waterway, Port, Coastal and Ocean Engineering*, ASCE, 134(6): 313-320.

Crespo, A.J.C., Dominguez, J.M., Gomez-Gesteira, M., Barreiro, A., and Rogers, B.D., (2012) “User Guide for DualSPHysics code.” DualSPHysics_v2.0,

http://www.dual.sphysics.org.

Crespo, A.J.C., Dominguez, J.M., Barreiro, A., Gomez-Gesteira, M. and Rogers, B.D. (2011) “GPUs, a new tool of acceleration in CFD: Efficiency and reliability on Smoothed Particle Hydrodynamics methods.” *PLoS ONE*, 6(6), *doi:10.1371/journal.pone.0020685*.

Dalrymple, R.A. and Rogers, B.D. (2006) “Numerical modeling of water waves with the SPH method.” *Coastal Engineering*, Elsevier, 53:141-147.

Dargahi, B. (1987) “Flow Field and Local Scouring around a Cylinder.” Royal Institute of Technology, Stockholm, Sweden, Bulletin No: TRITA-VBI-137.

Dey, S. and Raikar, R.V. (2007) “Characteristics of horseshoe vortex in developing scour holes at piers.” *Journal of Hydraulic Engineering*, ASCE, 133:399-413.

Dou, X., Jones, S., Young, G. K. and Sten, S. M. (1998) “Using a 3-D model to predict local scour.” *Proceedings of Water Resources Engineering Conferences*, ASCE, Memphis, Tennessee, USA, 198-203.

Edge, B.L., Overton, M.F., Dalrymple, R.A., Hérault, A., Bilotta, G., Kurum, M.O. and Gamiel, K. (2012) “Application of GPU Smooth Particle Hydrodynamics: Wave Runup and Overtopping on Composite Slopes.” *Coastal Engineering*.

FLUENT (1998), *FLUENT user’s guide manual,* version 5.0, Fluent Incorporated, Lebanon, N.H.

Gingold, R.A. and Monaghan, J.J. (1977) “Smoothed Particle Hydrodynamics: Theory and Appliaction to Non-spherical Stars.” *Monthly Notices of the Royal Astronomical Society*, 375-389.

Gomez-Gesteira, M. and Dalrymple, R.A. (2004) “Using a Three-Dimensional Smoothed Particle Hydrodynamics Method for Wave Impact on a Tall

Structure." *Journal of Waterway, Port, Coastal and Ocean Engineering*, ASCE, 130: 63-69.

Gomez-Gesteira, M., Rogers, B.D., Dalrymple, R.A. and Crespo, A.J.C. (2010) "State-of the-art of classical SPH for free-surface flows." *Journal of Hydraulic Research*, IAHR, 48: 6-27.

Gomez-Gesteira, M., Rogers, B.D., Dalrymple, R.A., Crespo, A.J.C. and Narayanaswamy, M. (2010) "User Guide for the SPHysics code." SPHysics_v2.0001, http://www.sphysics.org.

Gomez-Gesteira, M., Rogers, B.D., Crespo, A.J.C., Dalrymple, R.A., Narayanaswamy, M. and Dominguez, J.M. (2012a) "SPHysics – development of a free-surface fluid solver- Part 1: Theory and Formulations." *Computers & Geosciences*, Elsevier, 48: 289-299, doi:10.1016/j.cageo.2012.02.029.

Gomez-Gesteira, M., Crespo, A.J.C., Rogers, B.D., Dalrymple, R.A., Dominguez, J.M. and Barreiro, A. (2012b) "SPHysics - development of a free-surface fluid solver- Part 2: Efficiency and test cases." Computers & Geosciences, Elsevier, 48: 300-307, *doi:10.1016/j.cageo.2012.02.028*.

Graf, W.H. and Istiarto, I. (2002) "Flow pattern in the scour hole around a cylinder." *Journal of Hydraulic Research*, 40:13-20.

Groenenboom, P.H.L. and Cartwright, B.K. (2010) "Hydrodynamics and fluid-structure interaction by couples SPH-FE method." *Journal of Hydraulic Research*, IAHR, 48: 61-73.

Hopton, S. (2010) "Modelling Open Channel Flow." Thesis (PhD), University of Nottingham, UK.

Landers, M.N. and Mueller, D.S. (1996) "Channel scour at bridges in the United

States." Federal Highway Administration Report, FHWA RD 95-184.

Liu, G.R. and Liu, M.B. (2003) "Smoothed Particle Hydrodynamics a meshfree particle method." World Scientific Publishing Co. Pte Ltd.

Lucy, L.B. (1977) "A numerical approach to the testing of the fission hypothesis." *Astronomical Journal*, 82: 1013-1024.

Mendoza-Cabrales, C. (1993) "Computation of flow past a cylinder mounted on a flat plate." *Proceedings of Hydraulic Engineering Conference*, ASCE, Reston, Virginia, USA, 899-904.

Melville, B. W. (1975) "Local scour at bridge sites." *Report No. 117*, Department of Civil Engineering, School of Engineering, University of Auckland, Auckland, New Zealand.

Melville, B. W. and Raudkivi, A. J. (1977) "Flow characteristics in local scour at bridge piers." *Journal of Hydraulic Research*, 15:373-380.

Monaghan, J.J. (1992) "Smoothed Particle Hydrodynamics." *Annual review of Astronomy and Astrophysics*, Annual Reviews Inc., 30: 543-574.

Monaghan, J.J. (1994) "Simulating Free Surface Flows with SPH." *Journal of Computational Physics,* Elsevier, 110(2): 390-406.

Monaghan, J.J. and Kos, A. (1999) "Solitary waves on a Cretan beach." *Journal of Waterway, Port, Coastal and Ocean Engineering*, ASCE, 125: 145-154.

Randles, P.W. and Libersky, L.D. (1996) "Smoothed Particle Hydrodynamics: Some recent improvements and applications." *Computer Methods in Applied Mechanics and Engineering,* Elsevier, 139: 375-408.

Richardson, E.V. and Davis, S.R. (2001) "Evaluating scour at bridges." 4th ed., Federal Highway Administration, Hydraulic Engineering Circular No. 18,

Virginia, USA, FHWA NHI 01-001.

Richardson, J. R. and Richardson, E. V. (1993) “The fallacy of local abutment scour equations.” *Proceedings of Hydraulic Engineering Conference*, ASCE, Reston, Virginia, USA, 749-754.

Richardson, J.E. and Panchang, V.G. (1998) “Three-dimensional simulation of scour inducing flow at bridge piers.” *Journal of Hydraulic Engineering*, ASCE, 124:530-540.

Salaheldin, T.M., Imran, J. And Chaudhry, M. H. (2004) “Numerical modeling of three-dimensional flow field around circular piers.” *Journal of Hydraulic Engineering*, ASCE, 130:91-100.

Sarker, M.A. (1998) “Flow measurement around scoured bridge piers using Acoustic-Doppler Velocimeter (ADV).” *Flow Measurement and Instrumentation*, 9:217–227.

Shao, S. (2005) “SPH simulation of solitary wave interaction with a curtain-type breakwater.” *Journal of Hydraulic Research*, IAHR, 43(4):366-375.

Silvester, T.B. and Cleary, P.W. (2006) “Wave-structure interaction using Smoothed Particle Hydrodynamics.” *Fifth International Conference on CFD in the Process Industries*, CSIRO, Melbourne, Australia.

Shirole, A. and Holt, R. (1991) “Planning for a comprehensive bridge safety assurance program.” *Transportation Research Record*, 1290:137-142.

Staroszczyk, R. (2010) “Simulation of Dam-Break Flow by a Corrected Smoothed Particle Hydrodynamics Method.” *Archives of Hydro-Engineering and Environmental Mechanics,* 57(1): 61-79.

Tait, P. (1888) “Report on Some of the Physical Properties of Fresh Water and sea

Water." *Physical Chemistry 2*.

Takbiri, Z., Rasekh, A. and Afshar, M.A. (2010) "Analysis of Seepage through Dam Foundation using Smoothed Particle Hydrodynamics (SPH) Meshless Method." *World Environmental and Water Resources Congress 2010: Challenges of Change*, ASCE, 1604-1612.

Vacondio, R., Rogers, B.D., Stansby, P.K. and Mignosa, P. (2012) "SPH Modeling of Shallow Flow with Open Boundaries for Practical Flood Simulation." J*ournal of Hydraulic Engineering*, ASCE, 138: 530-541.

Verlet, L. (1967) "Computer Experiments on Classical Fluids I: Thermodynamical Properties of Leonard-Jones Molecules." *Physics Review*, 159: 98-103.

Yanmaz, A.M. and Altinbilek, H.D. (1991) "Study of time-dependent local scour around bridge piers." *Journal of Hydraulic Engineering*, ASCE, 117:1247 1268.

Wilcox, D.C. (1994) "Turbulence Modeling for CFD." *DCW Industries, Inc*.